UNIVERSITY OF OKLAHOMA

GRADUATE COLLEGE

THE DIURNAL CYCLE IN TROPICAL STORM ERIN (2007)

A THESIS

SUBMITTED TO THE GRADUATE FACULTY

in partial fulfillment of the requirements for the

Degree of

MASTER OF SCIENCE

by COLIN WELTY

Norman, Oklahoma

2026

THE DIURNAL CYCLE IN TROPICAL STORM ERIN (2007)

A THESIS APPROVED FOR THE
SCHOOL OF METEOROLOGY

BY THE COMMITTEE CONSISTING OF

Dr. James Ruppert (Chair)

Dr. Aaron Hill

Dr. Ben Schenkel

Acknowledgments

This research was supported by the National Science Foundation under Grant AGS-2331120. We first thank Robby Frost for his contributions to the manuscript in submission to Monthly Weather Review for this work. We also thank Dr. Clark Evans for feedback during the project, and Dr. Shun-Nan Wu, Dr. Rosimar Rios-Berrios, Dr. Yunji Zhang, and Emily Luschen for helpful feedback, discussions, and correspondence.

Table of Contents

List of Tables

List of Figures

Abstract

The diurnal cycle in post-landfall tropical cyclones (TCs) is sparsely studied, despite its implications for the timing and behavior of associated impacts, particularly in rare cases of overland re-intensification when poorly forecast nocturnal hazards occur. A noteworthy example is Tropical Storm (TS) Erin in 2007, which reached its maximum TC intensity over Oklahoma. Observational analysis shows that Erin intensified and produced its most intense rainfall nocturnally. We use convection-permitting Weather Research and Forecasting (WRF) simulations, including sensitivity tests that shift the solar diurnal cycle by 12 h, to show that this nocturnal timing is tied to the diurnal cycle. Additional simulations that impose surface fluxes from the control simulation separate the roles of atmospheric radiative forcing from surface-flux forcing tied to the nocturnal low-level jet (NLLJ). These experiments reveal a nocturnal preference for rainfall-rate maxima independent of NLLJ timing. However, vortex intensification more closely follows the nocturnal surface-flux phase. This difference is explained by convective organization relative to the radius of maximum winds (RMW): rainfall peaks are followed by stronger vorticity growth when low-level convergence and ascent are organized near or within the RMW. In the imposed-flux experiment, the later rainfall peak has a shallower boundary layer, stronger low-level convergence near the RMW, and stronger inner-core ascent than the earlier radiatively timed peak. These results suggest that radiative forcing modulates rainfall timing, whereas the surface-flux response helps determine whether convection is organized near the RMW and able to contribute to vortex intensification.

Chapter 1

Introduction

Tropical cyclones (TCs) are warm-core cyclones that primarily develop over tropical oceans and pose substantial threats to life and property, particularly when they make landfall. TC hazards include destructive winds, storm surge, tornadoes, and flooding, with rainfall often producing severe impacts well inland after landfall. Although considerable progress has been made in forecasting TC tracks, forecasting intensity change remains a major challenge (DeMaria et al., 2014). Therefore, further investigation into how tropical cyclones form, how they intensify, and how they interact with land surfaces is crucial for improved forecasting and reducing risk to life.

1.1 Tropical Cyclone Intensity

TC intensity is commonly described using maximum sustained wind speed and minimum sea-level pressure, with the Saffir–Simpson Hurricane Wind Scale classifying Atlantic hurricanes based on maximum sustained wind speed. Accurate prediction of TC intensity therefore requires understanding the processes that control changes in pressure, wind speed, and the organization of convection throughout the storm life cycle. Compared with TC track forecasts, which are strongly dictated by synoptic-scale steering flow, intensity forecasts depend on a complex combination of environmental conditions, storm-scale structure, air–sea or land–atmosphere exchange, and internal convective processes. One persistent challenge is rapid intensification (RI), in which

TC intensity increases quickly over a short period of time, typically defined as at least 30 knots in 24 hours. TCs that undergo rapid intensification are especially hazardous when they occur near landfall, as not only do they reach a higher intensity but often that intensity is not well forecasted, making resiliency and response for communities affected by landfall more challenging. However, RI is not the only challenge that remains with TC intensity forecasts.

TCs typically weaken after landfall due to increased surface friction, reduced surface enthalpy fluxes, and a general disruption of storm circulation (Kaplan and DeMaria, 1995; **?**; **?**). However, post-landfall TC behavior does not always follow this model of decay. A global analysis of inland TCs from 1979–2008 (Andersen and Shepherd, 2014) found that approximately 20% of TCs inland maintained or increased their strength after landfall, including warm-core, cold-core, and hybrid cases. These events are often associated with increased environmental moisture and increased soil moisture, allowing for a more barotropic environment. Additionally, predecessor rain events can rapidly onset these favorable conditions, leading to more significant rain accumulations (**?**). Therefore, while decay is a common behavior for TCs after landfall, it is possible for TCs to persist inland or, in rare cases, even intensify when conditions are favorable.

1.2 Tropical Cyclone Rainfall

One of the primary hazards associated with TCs, especially with regards to landfall, are heavy rainfall rates. Heavy rainfall rates can contribute to flooding that can extend well inland from the coast. While maximum wind speed and pressure is commonly used to describe TC intensity, rainfall can often produce impacts that are not captured by common intensity metrics. For example, inland rainfall hazards can occur even when TCs are weakening overland, making precipitation forecasts extremely critical for communicating the threat a TC poses after landfall (Lamers et al., 2023). As such, understanding the timing, magnitude, and spatial coverage of rainfall associated with TCs is essential for improving forecasts. Rainfall rates are also dynamically important because they provide an observable signature of convection within a TC. Deep convection releases latent heat, which can modify the circulation, size, and structure of a storm. In a TC context, diabatic heating is closely tied to secondary-circulation changes, pressure falls, and vorticity evolution relevant to vortex spinup (Adler and Rodgers, 1977; Schubert and Hack, 1982; Smith and Montgomery, 2016). Therefore, rainfall serves as a useful proxy for the timing and location of diabatic heating within a storm. Despite this connection, heavy rainfall and vortex intensification are not necessarily coupled. TCs can produce substantial rainfall without a corresponding increase in intensity. Previous work has shown that the placement of diabatic heating within a storm is important for determining the vortex response, with heating located closer to the inner core or within the radius of maximum winds (RMW) generally producing a stronger response than heating displaced farther outward (Musgrave et al., 2012; Smith and Montgomery, 2016). Thus, rainfall plays an important role both temporally and spatially in diagnosing TC behavior, with the location of rainfall relative to the inner vortex often being as important as the timing of the rainfall itself. Because rainfall exists as both a hazard and a proxy for convection, TC precipitation is likely very important for overland TC behavior. The timing of rainfall affects the evolution of inland hazards, while the spatial distribution of rainfall reflects how convection is organized within the storm. Again, this separation is important because convection within the RMW is more likely to intensify the circulation than convection distributed through outer rainbands. Therefore, understanding the links between TC rainfall and intensity requires considering both the timing of precipitation and its organization relative to the storm center.

1.3 The Tropical Cyclone Diurnal Cycle

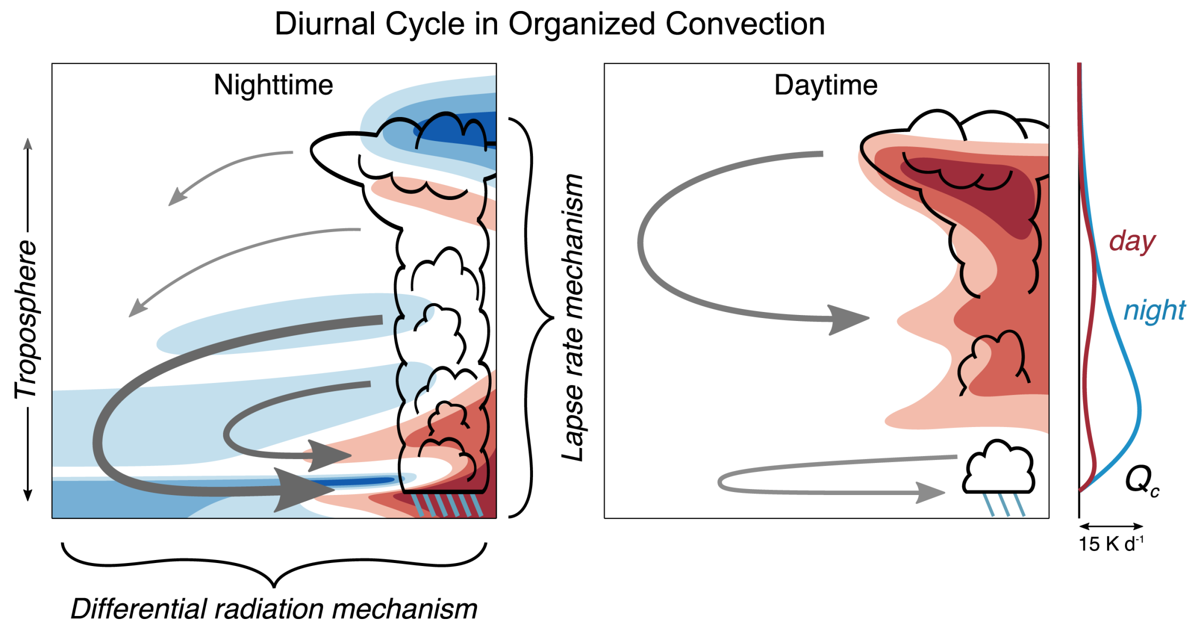

Figure 1.1: From Figure 10 in Ruppert and Hohenegger (2018), an idealized schematic of diurnal circulation adjustment between nocturnal (left) and daytime (right) convection in the tropics, highlighting the lapse rate mechanism and differential heating mechanism.

One potential source of predictability for TC rainfall and intensity change is the diurnal cycle. While the diurnal cycle within TCs has been studied for decades (Gray and Jacobson, 1977; Weickmann et al., 1977; Hobgood, 1986; Kossin, 2002; Dunion et al., 2014), recent work underscores that it may offer a reliable source of predictability for their behavior and impacts. For example, TCs that undergo RI show a preference for nocturnal intensification during periods of enhanced deep convection (Wu et al., 2020), consistent with how diurnal radiative forcing can modulate deep tropical convection (Ruppert and Hohenegger, 2018). In the framework proposed by Ruppert and Hohenegger (2018), depicted in Figure 1.1, there are two mechanisms that help to drive circulation changes between the daytime and nighttime phase of the diurnal cycle. In the absence of shortwave heating at night, the lapse-rate mechanism allows for an invigoration of deeper convection due to cloud-top cooling, leading to a nocturnal preference. The differential heating mechanism, characterized by the thermal difference between the cooler nocturnal environment and the warmer cloud regions, delays that peak to the early morning when the gradient peaks. In TCs, the diurnal cycle of radiative heating appears to favor earlier nocturnal convection near the eyewall with the delayed mechanism mattering more in the rainband regions (Evans and Nolan, 2022), highlighting the potential importance of storm structure in TCs. Additionally, this nocturnal convective enhancement has been linked to changes in low-level circulation, including enhanced boundary-layer inflow and low-level convergence (Ruppert and O'Neill, 2019; Zhang et al., 2020).

Satellite observations reveal regularly outward-moving "diurnal pulses" in the TC cloud canopy, which are argued to have impacts on various hazards, including extreme rainfall (Dunion et al., 2014; Ditchek et al., 2019; Zhang and Du, 2025). However, we do not yet understand if and how the role of these diurnal mechanisms changes upon making landfall as inland diurnal processes come into the picture. Studies such as Zhang et al. (2020) and Zhang et al. (2021) have shown that the diurnal cycle can affect the boundary layer in TCs, including with low-level convergence and asymmetric storm structure both over the ocean and near landfall. Therefore, the potential impacts of the diurnal cycle are likely critical for understanding not only rainfall timing, but also the organization of convection and vortex evolution during landfall events. Nonetheless, given little prior research on the diurnal variability in landfalling and overland TCs, we do not yet understand how TC diurnal variability changes after landfall, including the specific factors that dictate rainfall timing and intensity. Although past studies have documented the role of environmental factors in overland reintensification cases (Kaplan and DeMaria, 1995; Bosart and Lackmann, 1995; Xu, 2013), very few studies have analyzed the role of the diurnal cycle for controlling their specific diurnal timing.

We address this gap here with a focus on an extremely notable case – Tropical Storm (TS) Erin in 2007 – by leveraging numerical modeling experiments aimed at testing potential mechanisms.

1.4 Tropical Storm Erin (2007)

On 16 August 2007, TS Erin made landfall as a weak tropical storm in Lamar, Texas. The storm quickly weakened to a tropical depression during landfall and persisted as an area with organized convection embedded within a very moist plume of tropical air for several days. However, in the early-morning hours of 19 August, reintensification occurred over central Oklahoma into a tropical storm, complete with an eye-like structure and spiral rain bands, producing damaging winds exceeding 80 mph across central Oklahoma. At least 16 people were killed in the Great Plains due to hazards from the event, additionally causing substantial damage (Arndt et al., 2009). Real-time information on TS Erin's intensification was unique, since peak intensification occurred over the Oklahoma Mesonet. The high quality and spatial resolution of these measurements proved highly valuable for identifying its abnormal low pressure and rainfall intensity (Arndt et al., 2009).

A challenge in understanding any overland TC, including TS Erin, is the multitude of intertwined processes that may influence its evolution. Both observational and modeling studies have suggested that intensification was aided by a "brown ocean effect" (Andersen and Shepherd, 2014), resulting from above-average soil moisture as a result of months of above-average rainfall that permitted anomalously high surface evaporation (Arndt et al., 2009; Evans et al., 2011; Kellner et al., 2012). This scenario potentially supported intensification via wind-induced surface heat exchange (WISHE), which is a framework for interpreting TC intensification and maintenance both over ocean and land (Emanuel, 1986; Craig and Gray, 1996; Emanuel et al., 2008; Zhang and Emanuel, 2016). Another compounding factor is the nocturnal Great Plains low-level jet (NLLJ), a nocturnally-maximizing region of sustained southerly winds that peaks at approximately 1 km AGL and is associated with enhanced poleward moisture transport (Bonner, 1968). Previous studies on TS Erin have hypothesized that the NLLJ contributed to overland intensification, given the approximate match to the timing of intensification (Arndt et al., 2009; Evans et al., 2011). We test this hypothesis here.

1.5 Research Questions and Thesis Outline

TS Erin provides an ideal case from which to investigate the influence of the diurnal cycle on the timing and nature of overland TC intensification, especially given early morning rainfall maxima consistent with previous literature on precipitation timing (Bowman and Fowler, 2015). We thus conduct model simulations with mechanism-denial tests to to distinguish the roles of radiative forcing, surface enthalpy fluxes, and their diurnal timing, as well as revisiting external (i.e., synoptic-scale) factors for TS Erin's overland intensification that have been emphasized in previous studies. This thesis addresses two primary research questions:

1. Does the diurnal cycle dictate the timing of TS Erin's nocturnal, overland reintensification?

2. How does convective organization relative to the RMW within TS Erin modulate whether rainfall contributes to vortex spinup?

To answer these questions, we will execute phase-shift experiments for the radiative and surface-flux diurnal cycle to understand if shifting the clock similarly shifts the timing of intensification. To quantify changes in timing, our analysis focuses on rainfall rate and layer-integrated absolute vorticity to capture different elements of overland TC behavior. Rainfall is emphasized because its diurnal timing remains difficult to predict and because convection serves as a proxy for diabatic heating, which is central to TC maintenance and intensification (Adler and Rodgers, 1977; Schubert and Hack, 1982; Lamers et al., 2023; Smith and Montgomery, 2016). We therefore assess both the timing and location of rainfall relative to the vortex, particularly with regard to subsequent intensification.

Chapter 2

Data and Methods

2.1 Model Design

Our study consists of simulations using the Weather Research and Forecasting (WRF) model version 4.5 (Skamarock et al., 2019), forced using data from the fifth generation ECMWF reanalysis (ERA5) (Hersbach et al., 2020). The simulations were run on a two-nest grid (with two-way feedback) using an outer domain of 6-km horizontal grid spacing and an inner domain of 1.2-km spacing, with a stretched vertical grid of 64 levels. The study encompasses the broad timing of intensification for TS Erin from 21:00 UTC 17 August to 09:00 UTC 20 August 2007, with TS Erin's intensification peaking from 06:00–12:00 UTC 19 August in the real event.

This study leverages a model **Control** run intended to best represent the observed evolution of TS Erin, with modified-physics sensitivity tests intended to isolate the role of specific diurnal effects, as summarized in Table 2.1. Table 2.2 shows the chosen physics schemes as well as domain information, which is depicted in Figure 2.1. The sensitivity tests are identical to the **Control** run aside from the noted modifications (Table 2.1). To directly assess the role of the diurnal cycle in the timing of TS Erin's intensification, a primary sensitivity test, referred to as the **Diurnal** run, was undertaken using a 12-h shift to the solar radiation timing in the model. We did so by modifying the `calccozen()` function within the radiation driver physics module in

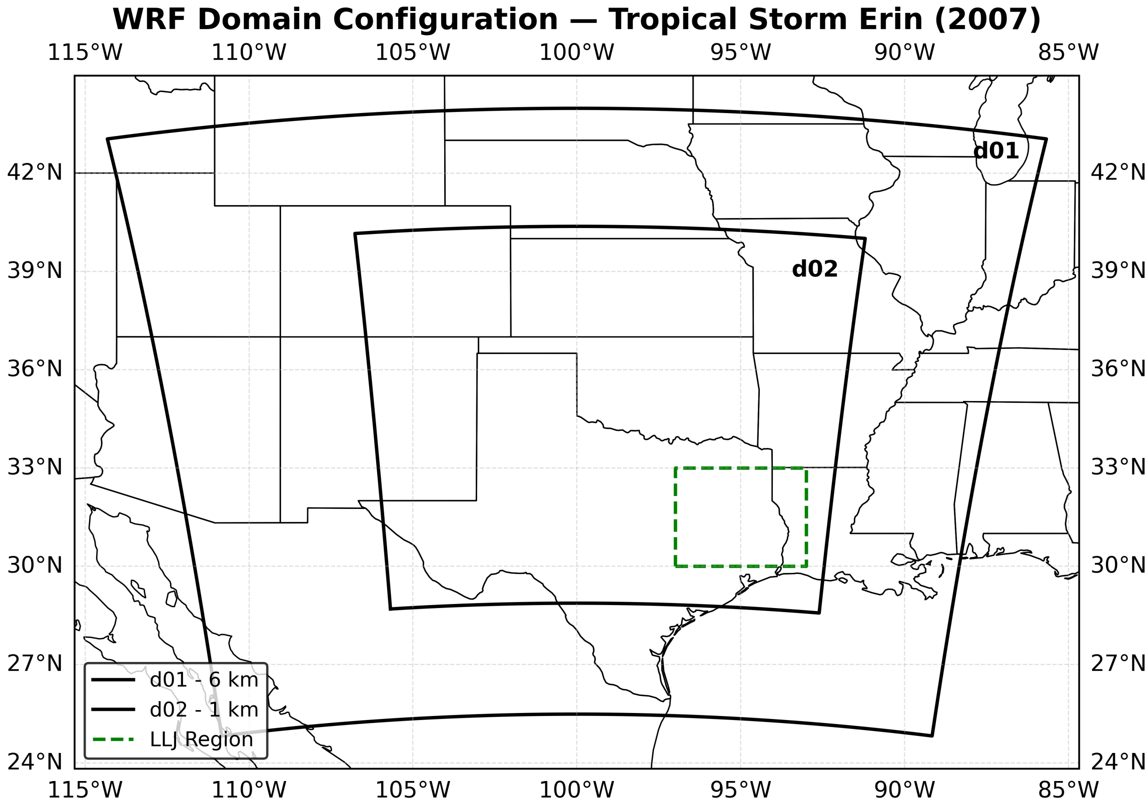

Figure 2.1: The inner (d02) and outer (d01) WRF domain configuration for the study alongside a dashed box demonstrating the region used for NLLJ capturing (green)

WRF (file name: `module_radiation_driver.F`). This modification shifts the diurnal cycles of atmospheric radiative forcing, interactive surface fluxes, and any other coupled diurnal processes. While the lateral boundary conditions were not modified in timing in these tests, this should not affect the inner model domain (Fig. 2.1).

The diurnal timing of the NLLJ in central Oklahoma is closely tied to the nocturnal transition of the boundary layer. From Blackadar (1957), the cooling in the nocturnal boundary layer is associated with a decay of turbulent mixing and an increase of static stability. The resulting reduction in turbulence allows for a decoupling of the flow at the boundary layer, allowing the ageostrophic wind to undergo an inertial oscillation and accelerate to being supergeostrophic. Holton (1967), however, theorized that the diur-

Table 2.1: Summary of the model experiments.

Simulation	Description
Control	Control simulation intended to mimic reality.
Diurnal	As in Control, but with the solar angle shifted by 12 h to invert the diurnal solar cycle.
C_imp1	Control with surface fluxes imposed from Control using the first imposition method.
C_imp2	Control with surface fluxes imposed from Control using the second imposition method.
D_imp1	As in Diurnal, but with surface fluxes imposed from Control using the first imposition method.
D_imp2	As in Diurnal, but with surface fluxes imposed from Control using the second imposition method.

Table 2.2: Summary of the model configuration used in all simulations.

Model setup	
Simulation duration	21:00 UTC 17 August–09:00 UTC 20 August
Horizontal grid spacing	6 km / 1.2 km for Domains 1 and 2, respectively
Vertical levels	64
Initial and boundary conditions	ERA5 reanalysis forcing (Hersbach et al., 2020)
Output frequency	Hourly
Physical schemes	
Cumulus parameterization	Grell–Freitas for d01 only (Grell and Freitas, 2014)
Planetary boundary layer	MYNN (Nakanishi and Niino, 2006)
Surface layer	MYNN (Nakanishi and Niino, 2006)
Land surface	Noah (Ek et al., 2003; Tewari et al., 2004)
Microphysics	Thompson aerosol-aware scheme (Thompson et al., 2008; Thompson and Eidhammer, 2014)
Shortwave radiation	RRTMG (Iacono et al., 2008)
Longwave radiation	RRTMG (Iacono et al., 2008)

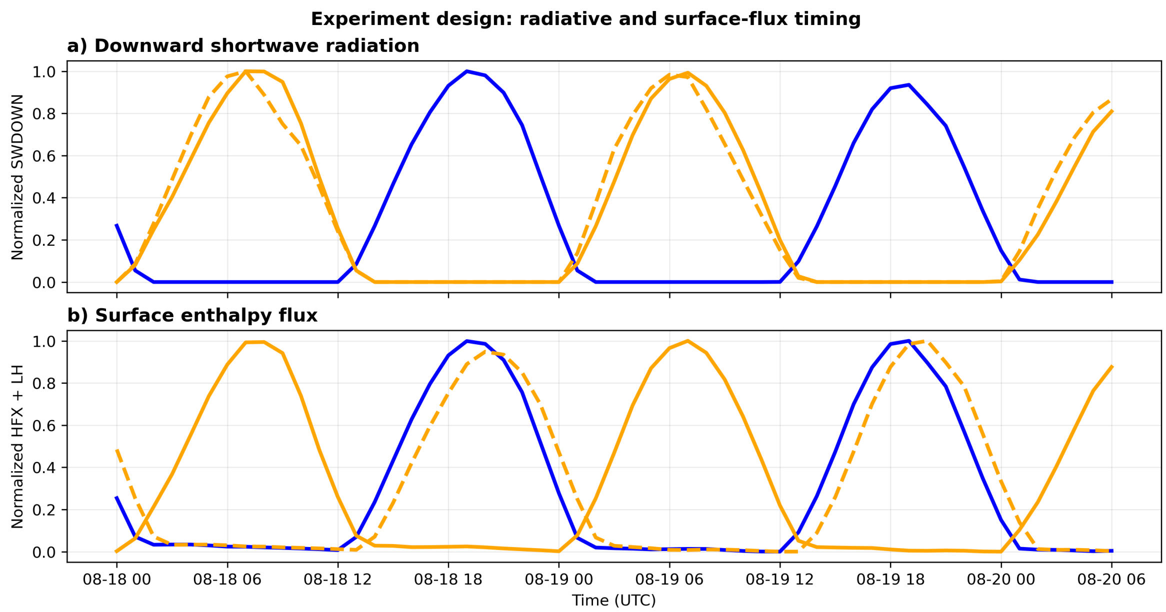

Figure 2.2: The experiment design conveyed through downward shortwave radiation (a) and surface enthalpy flux (b) for the Control (blue), Diurnal (solid orange), and D_imp1 (dashed orange) runs. The D_imp1 run follows the Diurnal radiative clock and the Control surface-flux clock.

nal heating gradient from the sloped terrain across the Great Plains provides enough forcing to drive southerly flow. Recent work has highlighted how both mechanisms are important, with temperature gradients providing sufficient forcing to generate an oscillation and the nocturnal boundary layer permitting an acceleration of this forcing, especially over Oklahoma (Du and Rotunno, 2014; Klein et al., 2016). Thus, surface fluxes play a key role in the diurnal variation of the NLLJ through modulating the nocturnal boundary layer. Because shifting the solar clock alters both the atmospheric radiative diurnal cycle and the diurnal response in surface fluxes, additional sensitivity tests are required to separate processes tied directly to atmospheric radiative forcing from those tied to surface fluxes, including the NLLJ. To that end, we conduct additional sensitivity tests where we impose the hourly surface fluxes taken from the **Control** run onto new runs, one pair with regular diurnal solar clock timing (**C_imp1**, **C_imp2**) and another pair with the 12-h solar cycle shift (**D_imp1**, **D_imp2**). We impose sensible heat flux (WRF variable name: HFX), water vapor flux (QFX), and latent heat flux (LH). This method of imposing previous WRF output onto a new run is implemented through I/O streams with modifications to the Registry and physics modules to ensure that the input fluxes overwrite the simulated fluxes at each model time step.

Since **Control** model output is saved hourly, surface fluxes are applied as constant values each model hour, updating each subsequent hour. Given the expected changes of fluxes over a one-hour time scale, we tested two approaches. In the first, fluxes were imposed from the corresponding **Control** run output hour (**C_imp1**, **D_imp1**), while in the second, fluxes were shifted back one hour so that values were applied leading up to their actual output time (**C_imp2**, **D_imp2**). In either case, this approach enables the radiative diurnal cycle to be shifted independently of the surface fluxes, as evidenced by the **D_imp1** following the diurnal run for radiative fluxes and following the **Control** for surface fluxes (Fig. 2.2).

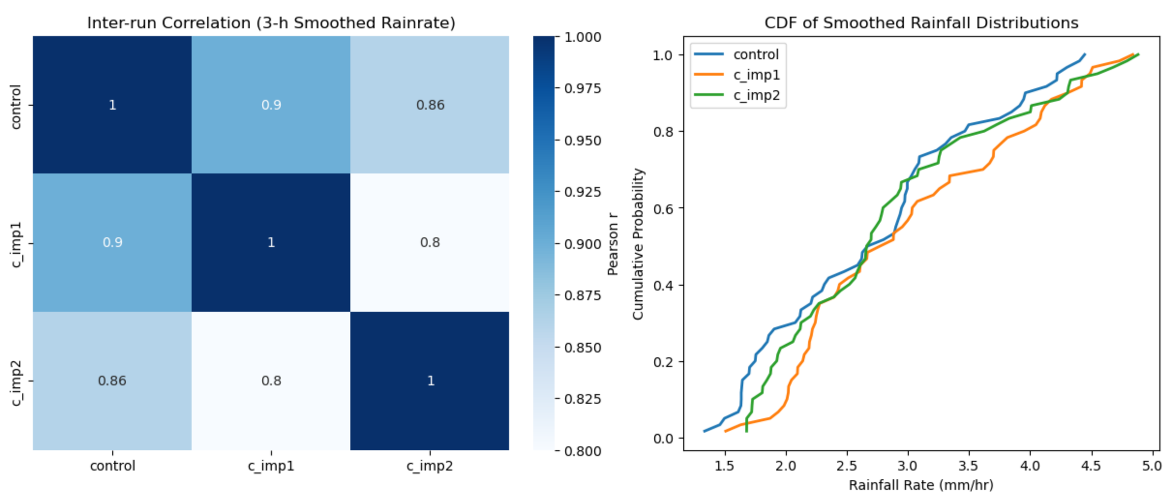

Figure 2.3: Statistical comparison of rainfall rate between the **Control** run and imposed methods using (left) pairwise Pearson correlations of the 3-h-smoothed rainfall-rate time series and (right) cumulative distribution functions of the corresponding smoothed rainfall rates.

The tests **C_imp1** and **C_imp2** serve to validate our method by replicating our **Control** run, but forced with these hourly-updating surface fluxes in place of the interactive fluxes. Figure 2.3 compares temporal rainfall correlations across these three runs, revealing that minor differences in the timing of imposing surface fluxes do not drastically alter the statistical character of rainfall rate within each run. As such, this study will display results from **D_imp1** when using spatial plots, for brevity.

2.2 Tracking and Analysis Framework

As mentioned in the introduction, we seek to examine and understand the distinct behaviors of rainfall and vorticity evolution associated with TS Erin's overland intensification. A key component of our analysis framework is therefore diagnosing processes associated with rainfall and vorticity in the vicinity of TS Erin, which requires tracking the model storm. TS Erin in each simulation was tracked using an object-based approach adapted from **?** and **?**. Relative vorticity maxima were first calculated at 3 km AGL from hourly model output. The vorticity field was smoothed in time and space using a 3-time-step by 9-by-9-point uniform filter and values exceeding 3 standard deviations were retained. The storm center at each time was defined as the vorticity-weighted centroid of the retained object, with the search constrained to remain within 5° latitude–longitude of the previous center to maintain temporal continuity. We compare the simulated tracks to the observed National Hurricane Center best track for TS Erin, obtained from the Atlantic HURDAT2 database (Landsea and Franklin, 2013), which ensures that our simulated storms follow approximately the same tracks (Figure A.1). Then, to localize our analysis to the track, a masking function is applied with a 2° latitude-longitude radius for rainfall, and a 1° latitude-longitude radius for absolute vorticity from each track point for each timestep. These radii were subjectively chosen from sensitivity testing to capture the different elements of TS Erin, with a larger radius used for rainfall rates to include outer rain bands associated with the cyclone (modest changes of these radii thresholds yield similar results).

We use the radius of maximum winds (RMW) throughout the analysis to distinguish inner-core convection from convection displaced radially outward. To do so, we compute the tangential wind at 10 m as $V_t = -u_{10}\sin\theta + v_{10}\cos\theta$, where θ is the azimuthal angle relative to the tracked storm center. We average V_t in 5-km radial bins and identify the RMW within a 10–150 km search radius. To reduce sensitivity to noise, the azimuthal-mean tangential-wind profile is smoothed with a 3-bin centered running mean, corresponding to a 15-km radial smoothing window. Because the maximum can be broad, we first identify the near-maximum region as all radii where the smoothed tangential wind is at least 95% of its maximum value. The RMW is then defined as the tangential-wind-weighted mean radius of those bins. We then apply an additional smoothing factor with a 3 h centered running mean. This approach places the RMW near the center of a broad wind maximum and reduces unnatural jumps between each time step.

To diagnose the vortex evolution and its drivers, we compute mass-weighted vertical means of absolute vorticity and vorticity-budget terms. For a variable A, the layer mean from level z_1 to z_2 is calculated as

$$\overline{A}^{\rho} = \frac{\displaystyle\int_{z_1}^{z_2} \rho A\, dz}{\displaystyle\int_{z_1}^{z_2} \rho\, dz}, \tag{2.1}$$

where ρ is air density, computed from model pressure, temperature, and water vapor mixing ratio. Absolute vorticity ζ_a is analyzed over 1–5 km AGL for the broader vortex response and over 0–1 km AGL for the low-level vorticity-budget analysis. The analysis leverages the vorticity-budget framework of Wang (2012), with minor modifications for the present storm-following analysis. First, the wave-relative horizontal flow $\mathbf{V}'$ in Wang (2012) is interpreted here as the storm-relative horizontal wind. For each simulation, the translation velocity of TS Erin, $\mathbf{C} = (U_c, V_c)$, is estimated from the change in track center location per hour, and this motion is subtracted from the model horizontal winds as $\mathbf{V}' = (u - U_c, v - V_c)$. Second, the budget is expressed in height coordinates rather than isobaric coordinates as

$$\frac{\partial \zeta_a}{\partial t} = -\nabla_h \cdot (\zeta_a \mathbf{V}') - \nabla_h \cdot \left(-w\mathbf{k} \times \frac{\partial \mathbf{V}}{\partial z} \right) + R, \tag{2.2}$$

where ∇_h is the horizontal divergence operator, $\mathbf{V} = (u, v)$ is the horizontal wind, w is the height-coordinate vertical velocity, $\mathbf{k}$ is the vertical unit vector, and R is the residual. Following Wang (2012), the first right-hand-side term is referred to as advective vorticity flux convergence and is associated with advection and the stretching of vorticity, while the second is referred to as nonadvective vorticity flux convergence and is associated with tilting of horizontal vorticity. Finally, the residual is diagnosed as the difference between the numerically computed time tendency term and the sum of the other computed right-hand-side budget terms.

Budget terms are first computed at each model output time at each grid point, then vertically averaged using mass-weighting over the 0–1 km layer. This follows a vorticity-budget framework motivated by prior studies of convectively driven TC spin up (Schubert and Hack, 1982; Wang, 2012; Smith and Montgomery, 2016). Next, the layer-mean fields are averaged into storm-centered radial bins. Budget terms are then integrated forward over the 6 h following each rainfall peak t_0 as follows:

$$\Delta A_{6h} = \int_{t_0}^{t_0+6h} A(t)\, dt. \tag{2.3}$$

The 6-h absolute-vorticity change is computed directly as

$$\Delta\zeta_a = \zeta_a(t_0 + 6h) - \zeta_a(t_0). \tag{2.4}$$

For RMW-relative summaries, values are area-weighted and averaged separately inside the RMW and outside the RMW. The inside-RMW region is defined from 15 km to the RMW, while the outside-RMW region is defined from the RMW to 200 km. For the storm-following spatial budget maps, each hourly field is shifted into a common storm-relative coordinate frame before the 6-h integration, so each grid point represents the same displacement from the tracked storm center throughout the integration window.

Local time (LT) references throughout this paper correspond to Central Daylight Time for central Oklahoma in August, or UTC−5 h. For experiments with the 12-h shifted solar cycle, we also refer to a radiative-clock local time, defined as LT + 12 h. Thus, the shifted radiative forcing corresponds equivalently to UTC+7 h. As such, LT should be thought of as corresponding to the solar diurnal cycle experienced in the simulation. For the imposed-flux experiments, we distinguish between the radiative clock, which follows the shifted solar cycle, and the surface-flux clock, which follows the **Control** run forcing.

Chapter 3

Results

This chapter establishes a two-pronged approach to addressing the questions in this thesis. The first step is to analyze the environment that TS Erin intensified in to ensure validity. The second is to provide evidence for answering the questions in chapter 1, with further discussion found in chapter 4.

3.1 Case Study Verification

3.1.1 Observational Analysis

A necessary step to place our study in a broader context is to assess whether intensification occurred alongside synoptic forcing, as well as highlight relevant environmental factors that helped set the stage for overland intensification. As mentioned in Evans et al. (2011), anomalously high soil moisture was observed as a result of persistent anomalous rainfall during the summer months leading up to TS Erin, promoting a brown-ocean effect and uncharacteristically enhanced surface enthalpy fluxes.

To understand the role of the NLLJ, we first show its evolution using time-height series of observed velocity-azimuthal displays (VADs) from WSR-88D radars and ERA5 reanalysis (Fig. 3.1). Comparing these data sources helps establish confidence that the reanalysis reproduces the observed low-level wind structures sufficiently for further comparisons to WRF data needed below. ERA5 generally captures the vertical struc-

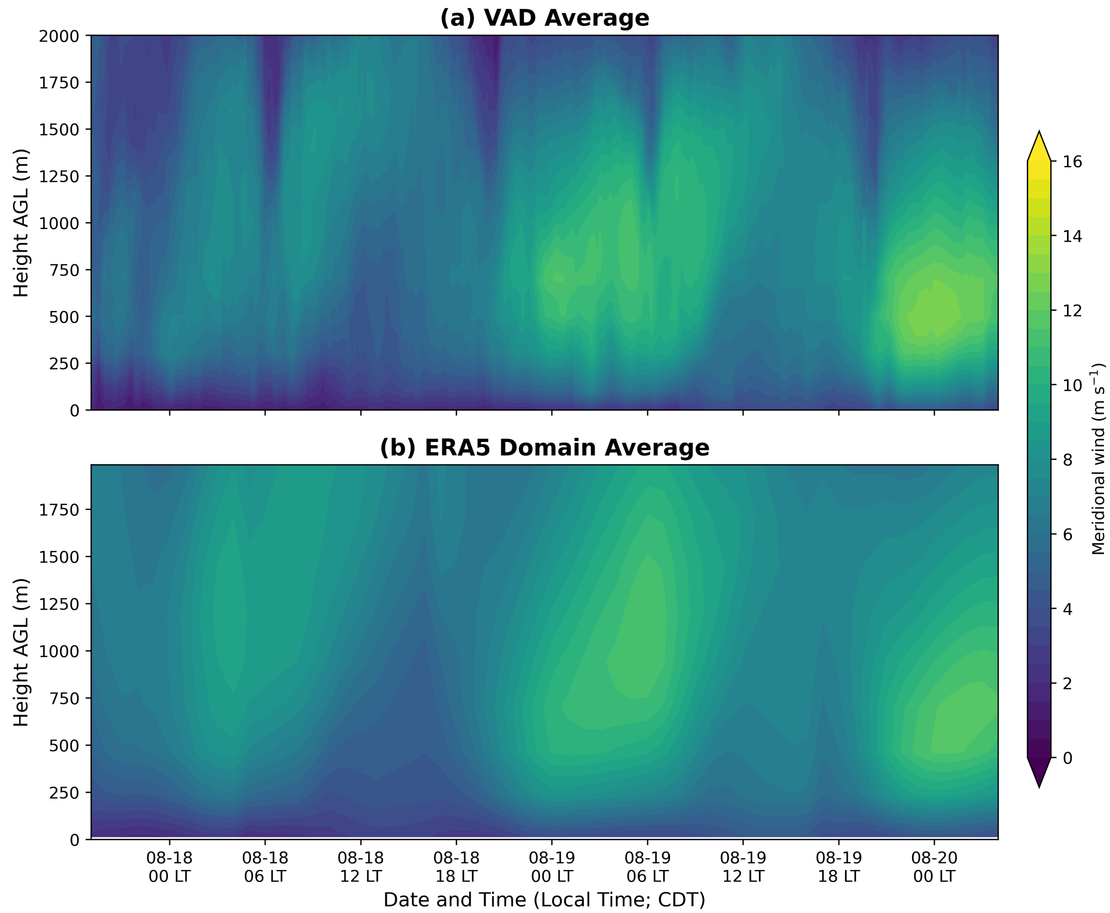

Figure 3.1: A time–height series of the meridional wind v during TS Erin's overland life cycle between (a) averaged velocity-azimuthal displays (VADs) retrieved from WSR-88D radars and (b) domain-averaged ERA5 reanalysis within 30 to 33° N and -97 to -93° W. The VADs are computed from radars at KFWS (Fort Worth, TX), KSHV (Shreveport, LA), and KLCH (Lake Charles, LA). For more information, refer to Figures 3.6 and A.3.

ture and timing of meridional winds observed in the VADs across the domain, with only minor differences in the magnitude of meridional winds at individual points. The VADs have maximum values around 15 m/s, which is approximately 2-5 m/s higher than ERA5, with the dominant maximum in both occurring during the night (early morning) of the 19th after TS Erin's intensification. This maximum on the 19th is about 1 km deep, extending from 1–2 km AGL. The observed NLLJ is collocated with

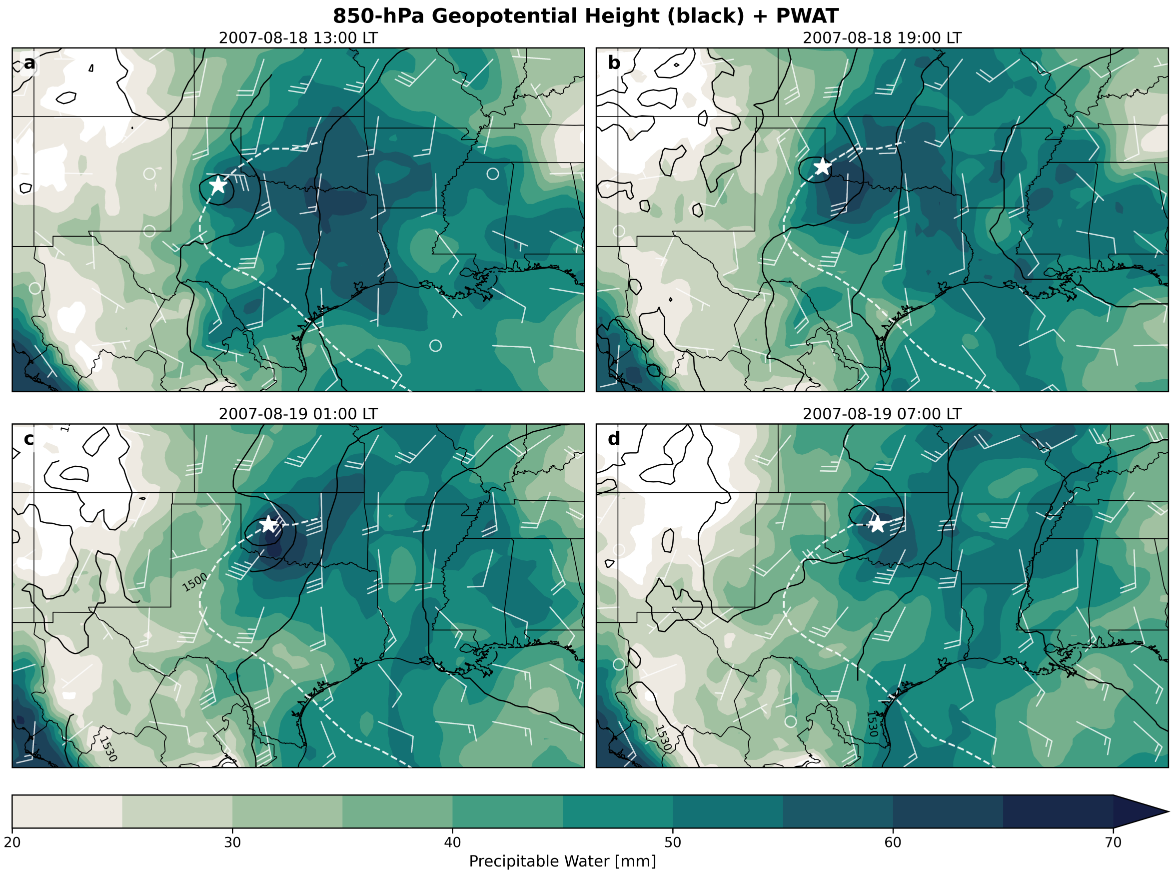

Figure 3.2: Six-hourly ERA5 precipitable water (PW) from 13:00 CDT on 18 August 2007 until 07:00 CDT on 19 August 2007. Geopotential height contours (black) and winds (white, full barb = 10 kts) at 850 hPa are overlaid. TS Erin's rainfall rate intensification approximately occurred between 00:00 CDT on 19 August and 06:00 CDT on 19 August. The white dashed line indicates TS Erin's track from HURDAT2 with the white star overlaying its position at each timestep.

the timing of TS Erin's overland intensification, signaling a potential link that we seek to untangle.

Significant moisture transport from the Gulf is carried out through two dominant features over the Southern Plains, as depicted in the map of ERA5 precipitable water (PW) and 850-hPa geopotential and winds (Fig. 3.2). The geopotential height field shows a rapidly tightening low pressure system associated with TS Erin that starts over western Texas during the early afternoon on 18 August, around 13:00 LT, which

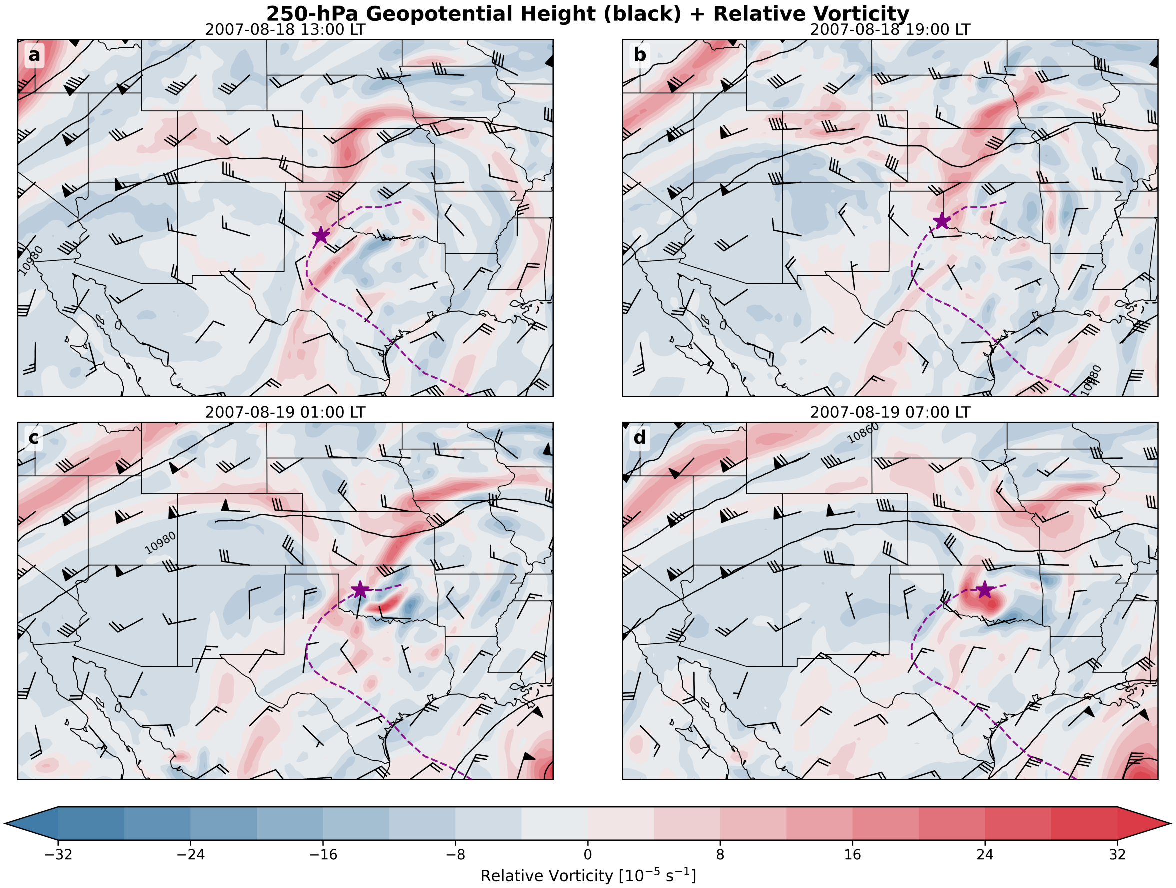

Figure 3.3: As in Fig. 3.2 but with relative vorticity shading, geopotential height contours, and winds at 250 hPa. TS Erin's track and position information is depicted in purple.

tracks into western Oklahoma by the early morning hours on 19 August, around 01:00–07:00 LT. PW values are elevated around TS Erin throughout the daytime and into the night of intensification. However, the area of eastern Texas and Oklahoma contains an initially distinct PW maximum (Fig. 3.2a) that broadens into the PW maximum associated with TS Erin from the afternoon of 18 August into the early morning of 19 August. This evolution is consistent with the argument that the NLLJ was important for supplying moisture to this region in advance of TS Erin's intensification (Evans et al., 2011).

Maps of 250-hPa relative vorticity and geopotential height show a large ridge in place over the Central Plains, with a small trough and cyclonic vorticity maximum along an approximately south–north line from the Big Bend region of TX through western KS in the day preceding and during intensification (Fig. 3.3). Based on this configuration, it is not straightforward to distinguish whether this quasi-linear upper-level cyclonic feature is independent and affects TC Erin's behavior or if it is a signature of the TC itself, similar to the "David effect" as noted by Bosart and Lackmann (1995). However, assessment of preceding flow patterns (not shown) reveal no tangible evidence of a notable predecessor trough associated with the features that appear in Fig. 3.3. Therefore, while this study does not aim to fully diagnose the causal role of synoptic-scale influences, the lack of clear evidence for a strong predecessor shortwave trough supports focusing on the potential role of local diurnal and land-surface processes as primary factors in the timing of TS Erin's re-intensification.

3.1.2 Model Comparison

While Section 3.1.1 aimed to understand the context of the environment within which TS Erin intensified, we next focus on our key WRF simulations to diagnose the role of the diurnal cycle on the timing of intensification. We begin by validating our **Control** run against observations. Figure 3.4 shows base reflectivity from Oklahoma City, Oklahoma (KTLX) alongside simulated reflectivity from the **Control** WRF run. A notable feature of TS Erin, both in observations and captured in our **Control** run, is the formation of an eye-like feature by 10:00 UTC (05:00 LT) on 19 August. While the eye-like feature is much more well-defined in observations than the simulation, important consistencies in these radar depictions include the asymmetry of TS Erin, with rainfall dominant on the east side of the storm; a singular spiral rainband with echoes exceeding 40 dBZ; and broad, weaker precipitation to the east of this primary rainband. We next present 24-h maximum wind and rainfall accumulations compar-

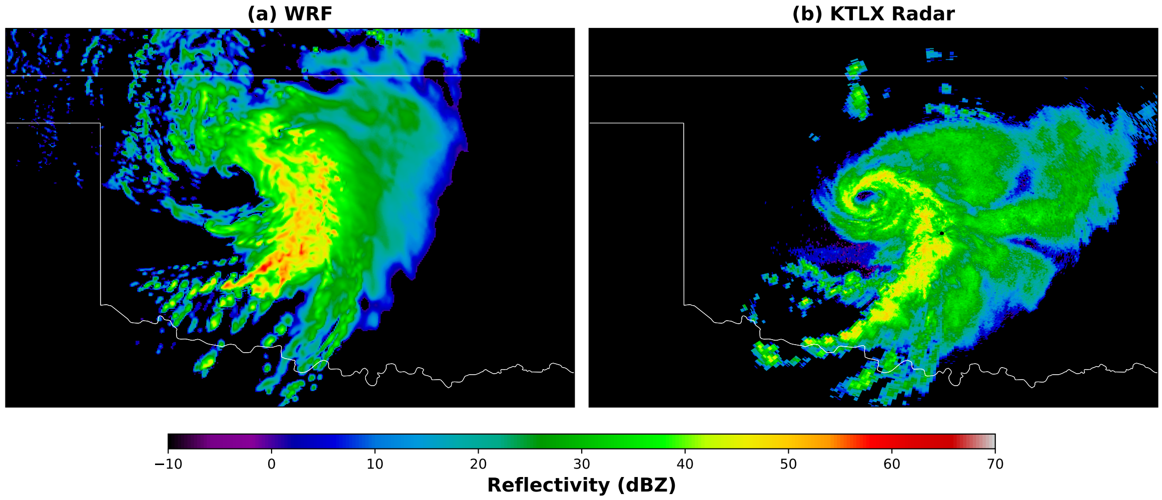

Figure 3.4: Comparison of reflectivity between (a) the WRF **Control** run and (b) the KTLX radar at 05:03 CDT capturing the cyclone during intensification over Oklahoma. A prominent eye-like feature is visible on both depictions over a similar location. Lowest-level elevation scan (0.5°) is used for KTLX and the lowest model level is used for WRF.

ing our **Control** simulation to NCEP Stage IV Quantitative Precipitation Estimates (Lin and Mitchell, 2005; Du, 2011) and wind speed observations from the Oklahoma Mesonet (Brock et al., 1995; McPherson et al., 2007) (Fig. 3.5). 24-h accumulated rainfall was aggregated between 1200 UTC 18 August and 1200 UTC 19 August 2007. The WRF rainfall field was sub-sampled by a factor of 2 in each horizontal direction, corresponding to an effective spacing of 2.4 km on the 1.2-km d02 grid, to provide a clearer comparison Stage IV rainfall field, which was plotted on its native grid without additional smoothing or interpolation. For the Mesonet comparison, station-based 24-h maximum wind speeds were interpolated to a 480×480 km latitude–longitude grid using cubic interpolation. The WRF 24-h maximum 10-m wind field was computed from hourly surface wind output and then smoothed using a 25-gridpoint maximum filter followed by a 25-gridpoint uniform filter, corresponding to an approximately 30-km window on the 1.2-km d02 grid.

Regions of heavy rainfall are generally similar between the simulation and obser-

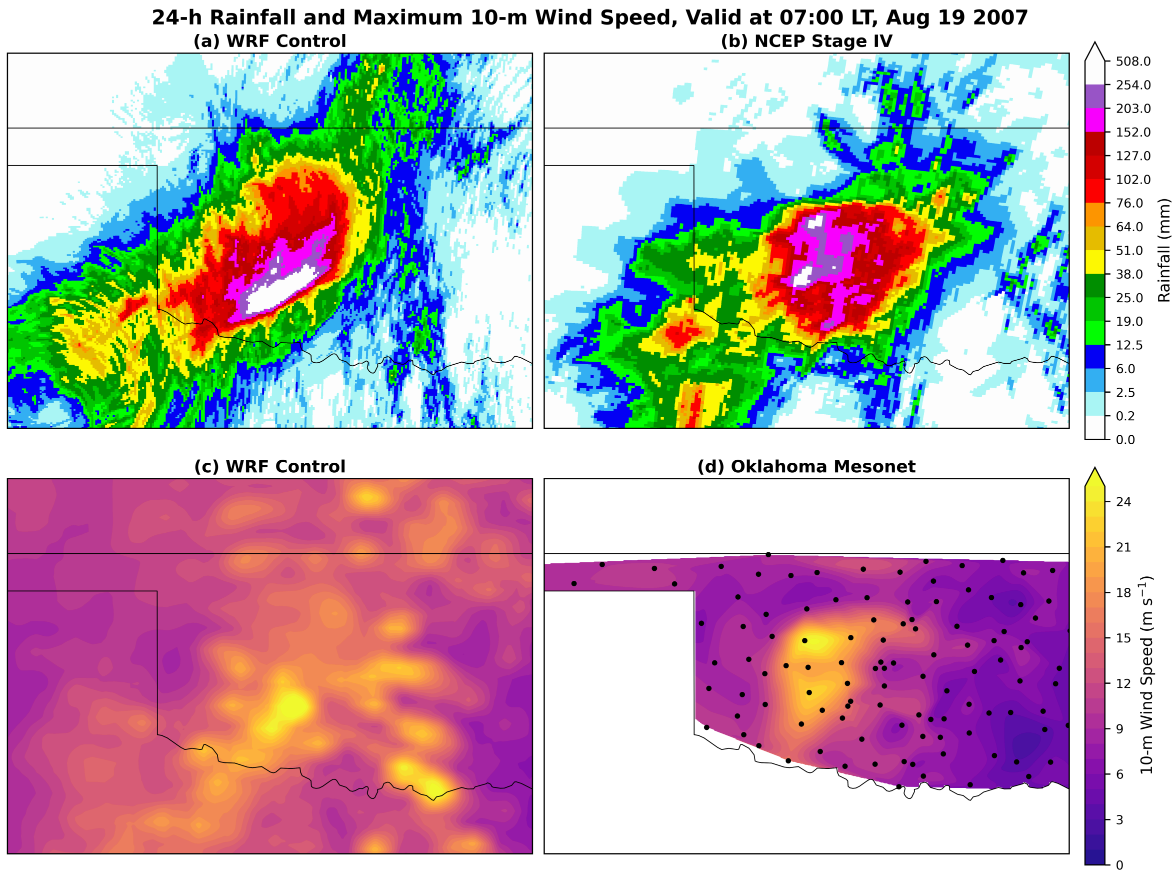

Figure 3.5: Comparisons of 24-h rainfall accumulations for a) the WRF **Control** and b) NCEP Stage IV Quantitative Precipitation Estimates and 24-h maximum 10-m wind speed for c) the WRF **Control** and d) observations from the Oklahoma Mesonet. Colorbar follows the NWS accumulation scale converted to mm. Rainfall data from the WRF **Control** is subsampled for visual comparison to NCEP rainfall data. 10-m wind speed in the **Control** run is smoothed with a gridpoint-based filter for visual comparison with Mesonet analysis. The period of data is from 12:00 UTC on 18 August–12:00 UTC on 19 August.

vations, with peak accumulation exceeding 250 mm in both (Fig. 3.5a,b). However, there is a more prominent northward extent to the simulated rainfall. Additionally, maximum amounts are located in similar areas within central OK for both datasets. The simulated rainfall maximum is, however, much broader spatially. 10-m wind speed maxima around 25 m/s are captured for both our **Control** run and Mesonet observations, though the location of wind maxima is again substantially broader in the **Control** run. Overall, the **Control** simulation models the impacts of TS Erin well based on these metrics, given similar maxima in both variables and the substantial spatial overlap in rainfall, although the simulation produces broader regions of the most intense wind speeds and rainfall.

Using the same tracking algorithm as that applied to **Control**, we next compare the track of TS Erin in all six runs to best track. As shown in Figure S3, for all cases, simulated tracks mimic NOAA Best Track data to a high degree. The **Control** deviates northward starting around 09:00 UTC on 19 August compared to observed. The **Diurnal** run moves slightly slower and with a bias towards the south, only moving north of the Best Track at about 21:00 UTC on the 19th. The other sensitivity tests lie within a few miles of each other.

These comparisons illustrate that our **Control** simulation of TS Erin is consistent with the real cyclone in terms of rainfall amounts, surface wind, and reflectivity signatures. We thus conclude that our **Control** run is sufficiently representative of the real-world scenario to justify examining the sensitivity tests to quantify TS Erin's sensitivity to diurnal forcing.

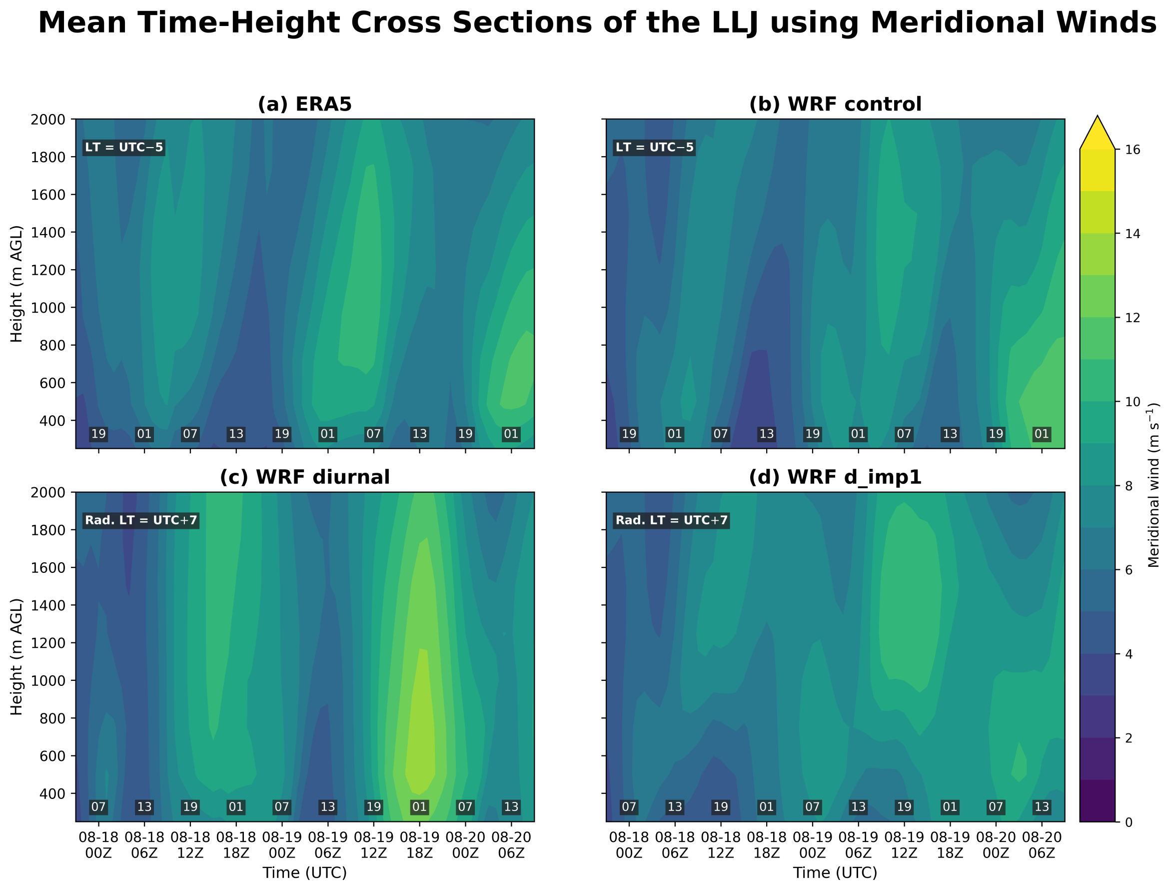

Figure 3.6: Time–height series of v-wind with a) ERA5, b) **Control**, c) diurnal, and d) D_imp1 from 250–2000 m AGL. For WRF, v-winds are interpolated to 250-m AGL height levels. The averaging domain is from 30–33° N and -97—93° W as referenced in Fig. A.2. LT is indicated at the inside-bottom of each sub-panel (note: this accounts for the shifted solar clock in the **Diurnal** run).

3.2 Model Analysis

3.2.1 Diurnal LLJ and rainfall timing

We next assess the NLLJ based on averages of the v-wind over Southeast Texas and Western Louisiana, comparing ERA5 reanalysis with the **Control** and two sensitivity simulations (Fig. 3.6). The **Control** run depiction of the NLLJ exhibits strong similarity to ERA5 in terms of diurnal timing and vertical structure, indicating that

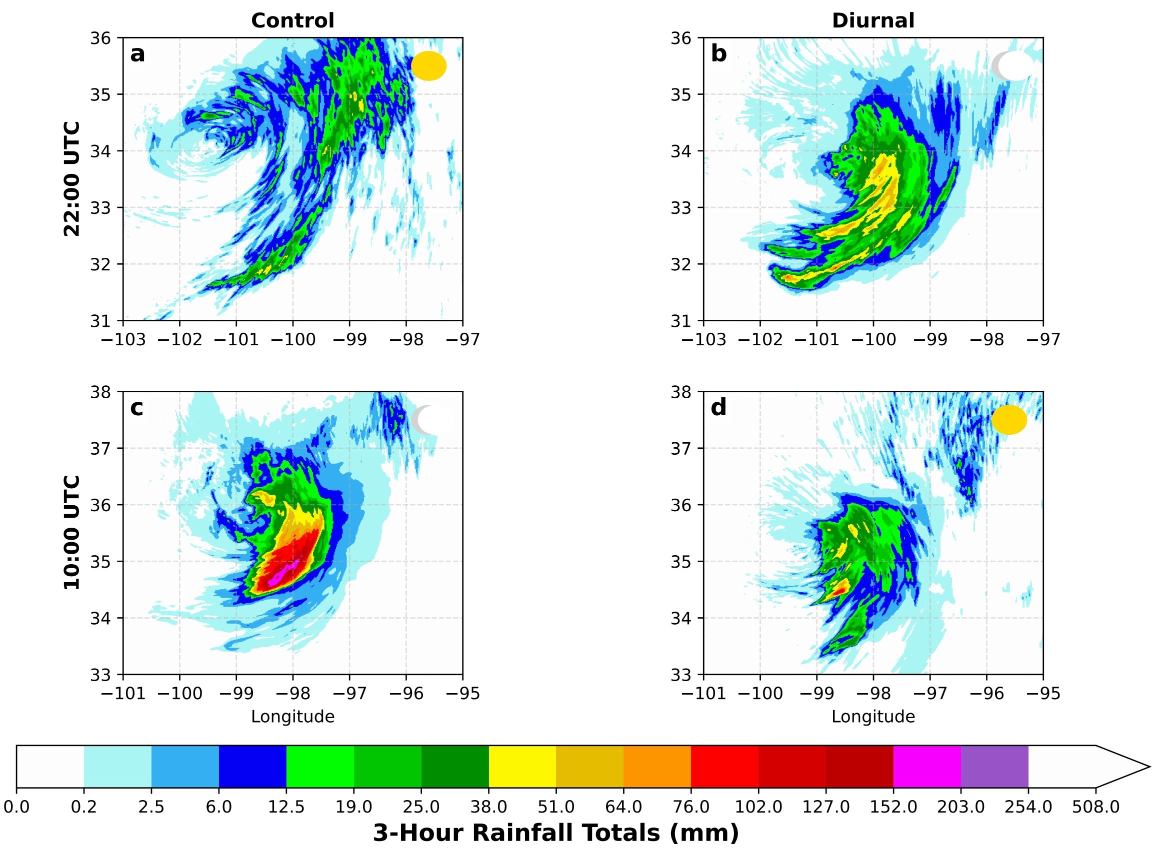

Figure 3.7: 3-h accumulated rainfall for **Control** (a, c) and **Diurnal** (b, d) simulations at 22:00 UTC on 18 August (a, b) and 10:00 UTC on 19 August (c, d). Moon and sun icons in top-right of each sub-panel denote if run is experiencing night (05:00 LT) or day (17:00 LT) atmospheric radiative forcing.

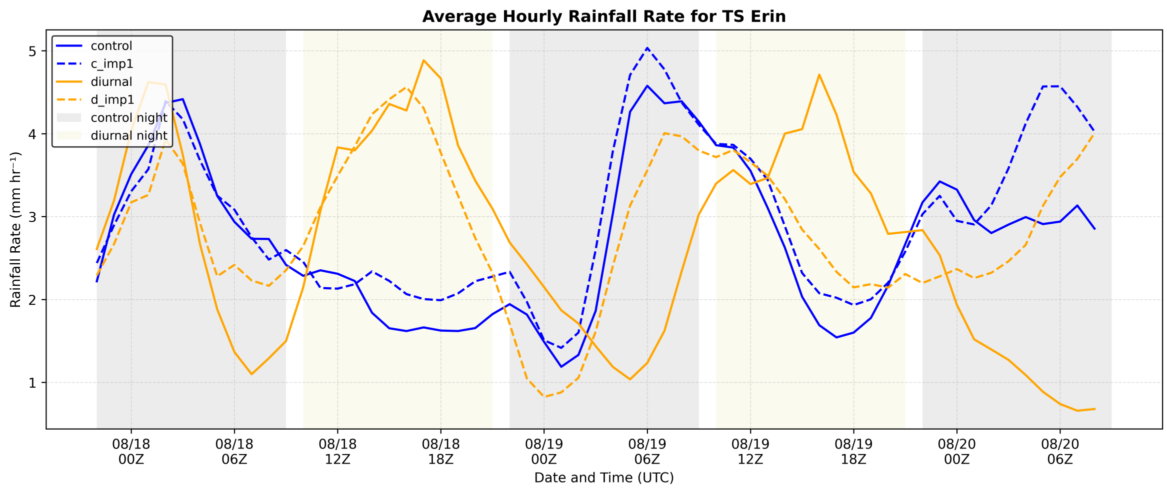

Figure 3.8: Time series of mean rainfall rate within a 2° latitude-longitude radius of the tracked TC center for six simulations. Nighttime for the **Control** experiments is shaded gray and nighttime for the **Diurnal** experiments is shaded beige.

this run has properly modeled the NLLJ. The diurnal run suggests that altering the clock similarly alters the timing of the NLLJ, with the NLLJ maximum shifted to approximately 13:00 LT on 18 August, compared to approximately 01:00 LT on 19 August in the LT clock of **Control**. Imposing the surface fluxes in **D_imp1** displays a NLLJ that more closely resembles the **Control** run rather than the **Diurnal** run. However, there is a difference in wind values in the lowest 500 m, indicative of some influence from the **Diurnal** radiative cycle, specifically around 13:00 LT on 19 August. In general, this shift is consistent with the interpretation that surface fluxes govern the diurnal timing of the nocturnal NLLJ, thereby indicating that our experimental framework effectively isolates the nocturnal NLLJ from the diurnal evolution of atmospheric radiative forcing.

To further compare the **Control** run and the **Diurnal** run, we next compare 3-h rainfall accumulations (Fig. 3.7). At 22:00 UTC on 18 August, the **Control** run has evidence of a vortex through a spiral rainband feature, but rainfall accumulations are lower than the **Diurnal** run (Fig. 3.7a,b). However, at 10:00 UTC on 19 August, the

Control run has much larger rainfall totals compared to the **Diurnal** run, which has weakened in terms of overall magnitude and raining area. These results are consistent with a nocturnal rainfall preference, which is further examined below.

To assess the direct effects of the diurnal cycle of solar heating, we analyze our simulations using time series of masked-mean rainfall rates. Figure 3.8 shows the time series of mean rainfall rate within a 2° latitude-longitude radius of TS Erin for our four experiments. All runs display a clear nocturnal rainfall maxima, consistent with the rainfall accumulation maps depicted in Fig. 3.7. The **Diurnal** run exhibits prominent peaks on 18 and 19 August that occur roughly 12 hours out of phase with the **Control**. **C_imp1** exhibits robust similarities to the **Control** run, with only minor differences in magnitude. The overall consistency provides confidence in the method of imposing surface fluxes as applied in the other tests.

Diurnal and **D_imp1** also exhibit primary peaks at their nocturnal hours across all three sensitivity tests. However, **D_imp1** also exhibits a local rainfall maximum on 19 August that aligns with that of the **Control** run, albeit slightly delayed and weaker. Therefore, **D_imp1** exhibits two rainfall peaks in 24 hours, implying that the timing of both surface-flux forcing and atmospheric radiative forcing influences diurnal rainfall intensity in this experiment.

Furthermore, the 18 August rainfall maximum in the **D_imp1** is consistent with the peak found in the **Diurnal** run, while the NLLJ timing approximately matches that of the **Control** in these tests. This indicates that the NLLJ alone cannot explain the nocturnal rainfall peak that appears on 18 August in the **Diurnal** and **D_imp1** runs (Fig. 3.6). However, the secondary peak in **D_imp1** aligns more closely with the **Control** rainfall maximum, albeit slightly offset. The explanation for this feature is likely positive feedback between our imposed surface fluxes from the **Control** and precipitation. We next investigate the question of if and how these rainfall peaks relate

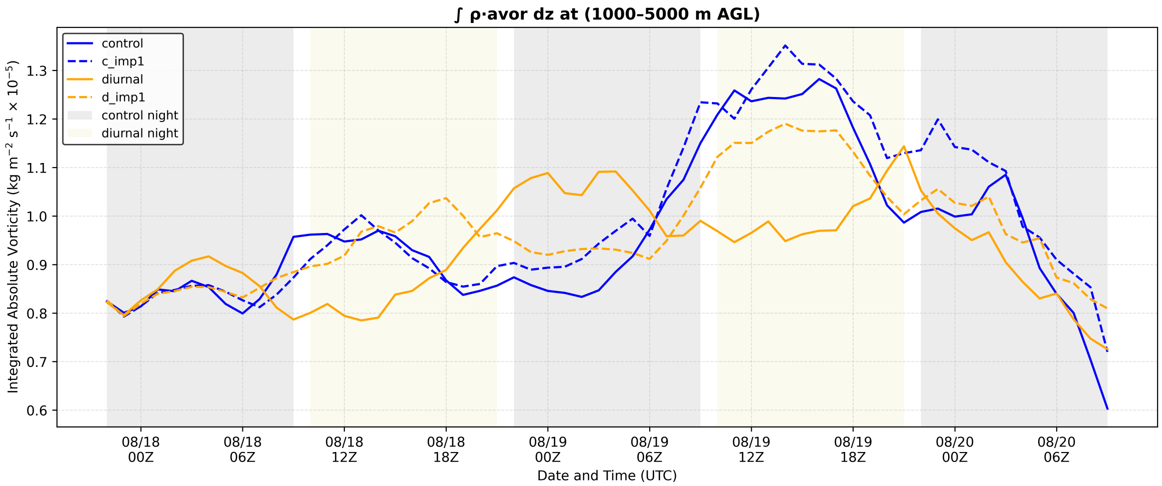

Figure 3.9: As in Fig. 3.8, except showing the mass-weighted vertical mean absolute vorticity (AVOR) between 1–5 km AGL.

to the evolution of vorticity.

3.2.2 Absolute vorticity

To diagnose vortex behavior, we next plot the mass-weighted vertical mean of absolute vorticity from 1000–5000 m and compare its time evolution across the different simulations (Fig. 3.9). A clear phase shift is seen between the **Control** run and the **Diurnal** run, indicating that diurnal changes affect the timing of absolute vorticity. Absolute vorticity is approximately in quadrature with rainfall rates, peaking in the early morning at approximately 05:00 to 08:00 LT for the **Control** run (12:00-15:00 UTC) and the **Diurnal** run (00:00 to 03:00 UTC). This is consistent with the role of low-level convergence coupled to this precipitation in intensifying the vortex (Smith and Montgomery, 2016). While the **C_imp1** run approximately mirrors the **Control** run in timing, the **D_imp1** run deviates from the **Diurnal** run, instead following the intensification timing of the **Control** run. Across the experiments, the behavior of absolute vorticity appears closely linked to the diurnal timing of the surface fluxes and the timing of the NLLJ. The variation between **D_imp1** rainfall timing and vorticity timing, however, motivates looking into the structure of TS Erin to identify where and how the separated diurnal cycles affects its behavior.

3.2.3 Convective organization and RMW vortex response

A notable feature of the diurnally imposed suite of simulations is the emergence of two independent rainfall peaks within 24 hours, with the first at 18:00 UTC 18 August (01:00 LT), which is during the radiative nighttime and surface-flux daytime, and another at 06:00 UTC 19 August (13:00 LT), which is during the radiative daytime and surface-flux nighttime. Given the experiment design (Fig. 2.2), the first rainfall peak in the **D_imp1** runs is attributable to the shifted radiative clock, whereas the second peak is consistent with a response to the diurnal cycle of the surface flux imposition. Analysis of the distribution of convection illustrates a major difference in the structure of TS Erin between the two peaks. Figure 3.10 shows lowest-model-level reflectivity 3 h after the primary rainfall peaks. This lag is chosen to compare the convective structure during the period between the rainfall maximum and subsequent vorticity response. In the **Control**, **Diurnal**, and second **D_imp1** peak, reflectivity remains concentrated near the RMW with asymmetric structure (Fig. 3.10a,b,d) and a smaller RMW field. The first **D_imp1** peak, however, has less convective reflectivity within the RMW and is characterized by a broader spiral rainband displaced outward from the inner core (Fig. 3.10c), with a much larger RMW field. Thus, while spiral reflectivity features are present in all cases, the first **D_imp1** peak is structurally different from the other rainfall peaks because convection is less collocated with the RMW.

This difference in convective organization relative to the RMW is significant because convection located within the RMW should more efficiently allow diabatic heating to generate a vorticity response than convection located outside the RMW in the outer

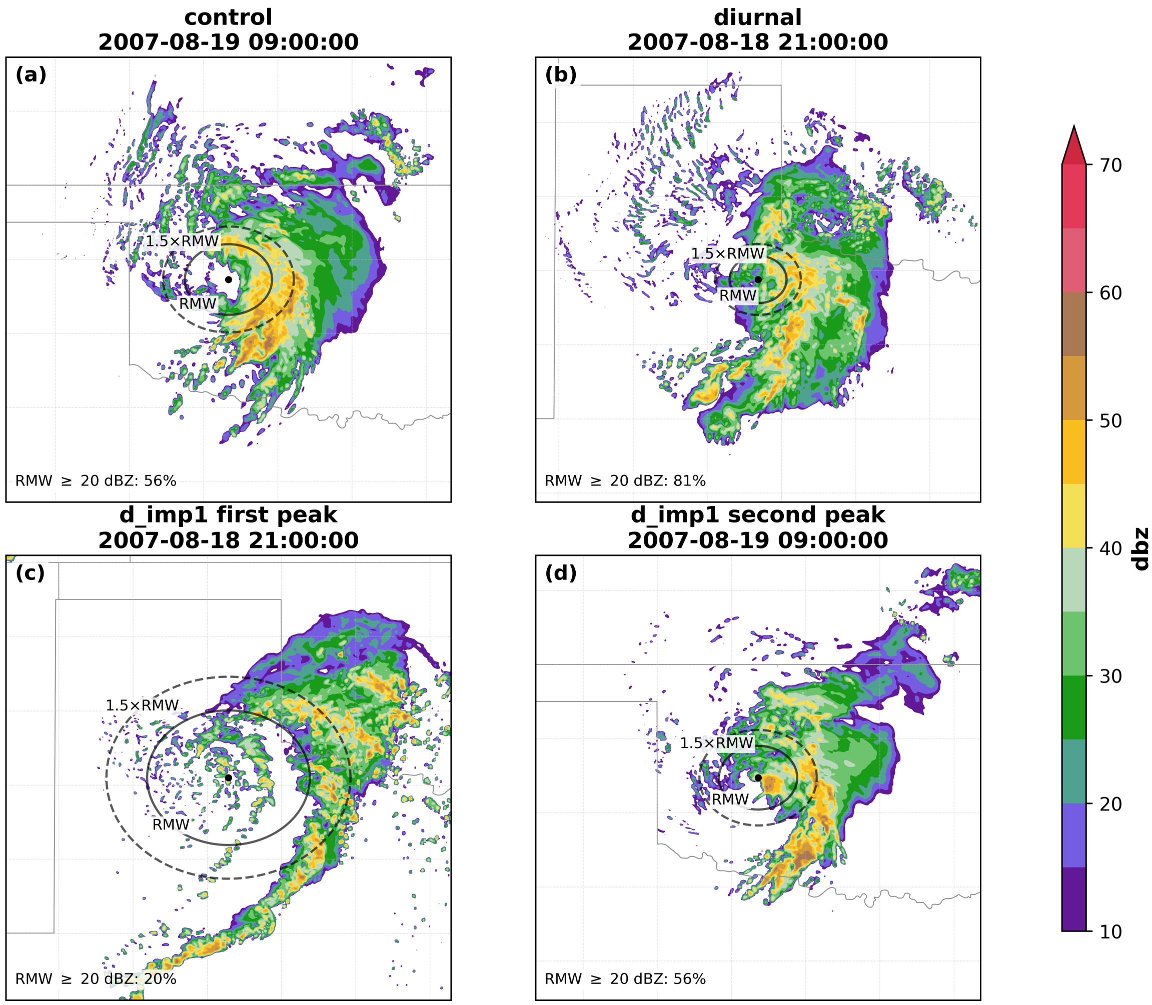

Figure 3.10: Lowest-model-level reflectivity 3 h after the primary rainfall peaks in (a) Control, (b) Diurnal, and (c,d) D_imp1. Panels (b) and (c) show the Diurnal and D_imp1 structure at 21:00 UTC on 18 August (04:00 LT), and panels (a) and (d) show the Control (04:00 LT) and D_imp1 (16:00 LT) structure at 09:00 UTC on 19 August. Solid and dashed circles denote the RMW and 1.5×RMW, respectively.

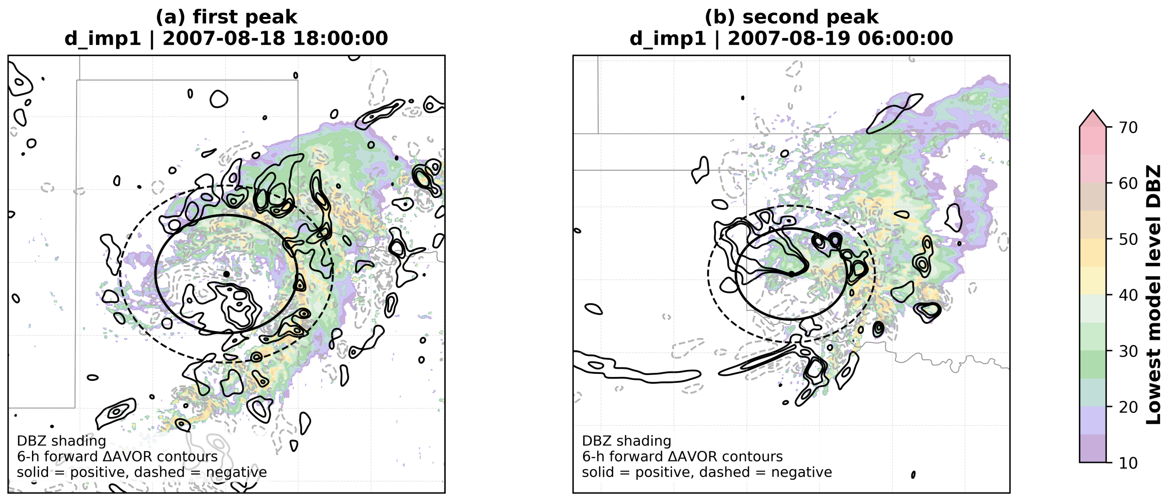

Figure 3.11: Lowest-model-level reflectivity at the two **D_imp1** rainfall peaks, overlaid with contours of the subsequent 6-h change in 0–1-km layer-mean absolute vorticity (ΔAVOR; 10^{-5} s^{-1}). Contours are plotted at ±1, ±2.5, ±5, and $\pm10 \times 10^{-5}$ s^{-1}, with solid black contours denoting positive ΔAVOR and dashed gray contours denoting negative ΔAVOR. The solid circle marks the RMW, and the dashed circle marks 1.5$\times$RMW, as in Fig. 3.10.

rainbands. Figure 3.11 shows reflectivity and forward-integrated absolute vorticity for the two **D_imp1** rainfall rate peaks. While both peaks have positive and negative vorticity generation within the RMW, the peak at 18:00 UTC 18 August (01:00 LT) has mostly negative 6-h vorticity change overlapping with DBZ in the RMW, with positive vorticity primarily overlapping outside the RMW or in rain-free regions. In contrast, the peak at 06:00 UTC 19 August (13:00 LT) has tighter collocation of positive absolute vorticity increase within and around the RMW. As noted in Fig. 3.9, the first peak generates a significantly weaker increase in vorticity compared to the second peak. The differences between the two peaks support that the response of absolute vorticity from convection is attributable to the location and organization of that convection relative to the vortex. Figure 3.12 displays the change in the vorticity budget terms alongside 6-h rainfall rate with respect to the RMW. Overall, the nocturnal peaks that have higher rain rate inside the RMW are followed by positive 6-h changes in absolute vorticity and

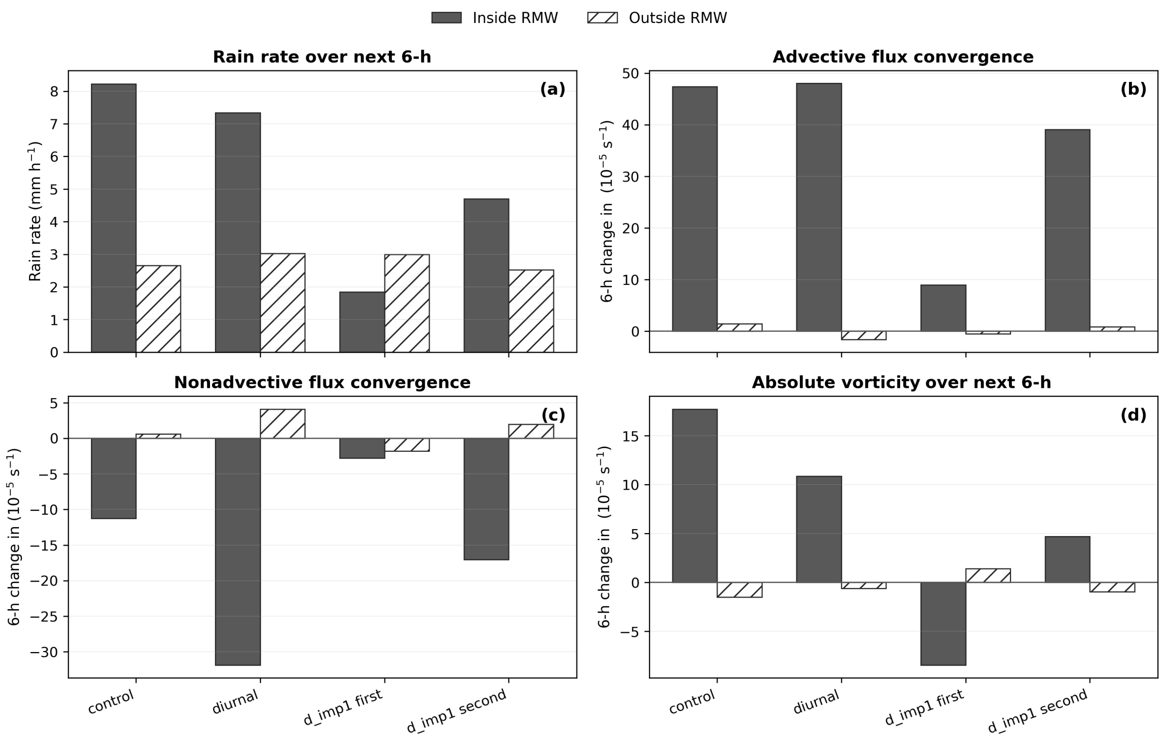

Figure 3.12: Rainfall rate and 0–1-km vorticity-budget terms averaged inside and outside the RMW for the primary rainfall peaks for each run: 18:00 UTC 18 August for **Diurnal** and **D_imp1** first peak; 06:00 UTC 19 August for **Control** and **D_imp1** second peak. Bars show the rain rate over the following 6 h (a), 6-h integrated advective (b) and nonadvective flux convergence (c), and the corresponding 6-h change in absolute vorticity (d). Filled bars indicate values inside the RMW and hatched bars indicate values outside the RMW.

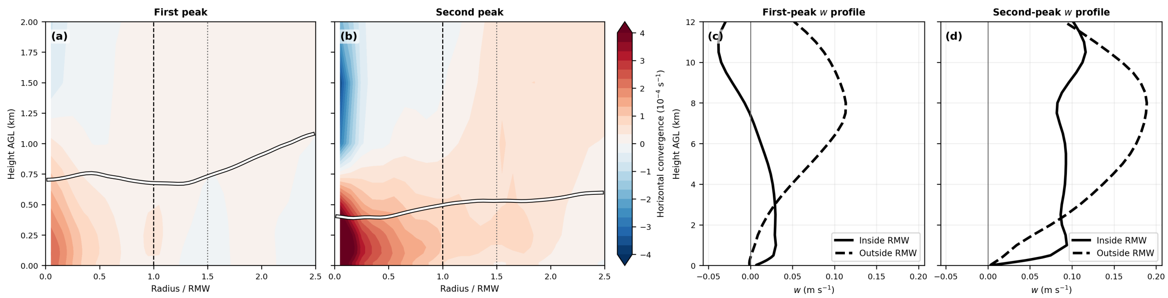

Figure 3.13: 6 h mean low-level horizontal convergence and vertical profiles for the two **D_imp1** rainfall peaks. The first peak occurs during radiative night / imposed surface-flux day, while the second occurs during radiative day / imposed surface-flux night. Shading in (a) and (b) shows horizontal convergence (10^{-4} s^{-1}) from 0–2 km AGL for the first and second **D_imp1** peaks, respectively, with positive values denoting convergence. The thick black line denotes the PBL height for each run, derived from the MYNN PBL scheme. The vertical dashed lines mark the RMW. Panels (c) and (d) show area-weighted vertical profiles of w for the first and second **D_imp1** peaks, respectively. Solid lines denote values averaged inside the RMW and dashed lines denote values averaged outside the RMW.

advective flux convergence. The lone exception is the first **D_imp1** peak, which has higher rainfall rates outside the RMW (Fig. 3.12a). Similarly, the first **D_imp1** peak has markedly weaker positive advective flux convergence, which includes horizontal vorticity advection and stretching. Additionally, while the other three rainfall peaks have a subsequent increase in absolute vorticity within the RMW, the first **D_imp1** peak has a decrease in absolute vorticity over the following 6 h. These panels reinforce the idea that the location of convection relative to the center of TS Erin dictates whether rainfall is dynamically efficient for vortex spin-up. In the first **D_imp1** peak, the rainfall maxima are radially displaced outward from the RMW, producing little vorticity growth, whereas the second peak produces a vorticity response with inner-core convection.

While Figs. 3.10–3.12 demonstrate that the first and second **D_imp1** peaks differ in their convective organization and subsequent vortex response, they do not directly show how the imposed surface-flux phase may affect that organization. To further diagnose this, we plot 6 h mean low-level horizontal convergence and vertical profiles for the two **D_imp1** rainfall peaks in Figure 3.13. Compared to the first peak, the second peak is characterized by a shallower PBL and stronger low-level convergence near the RMW. This difference in low-level convergence is accompanied by a stronger vertical-motion response within the RMW, with the second peak exhibiting larger positive w through much of the lower and middle troposphere. In contrast, the first peak has weaker ascent within the RMW and additional weak descent aloft, while the stronger ascent is primarily located outside the RMW, consistent with the structure shown in Fig. 3.10. The shallower PBL combined with the stronger low-level convergence within the RMW suggests that the night phase of the surface-flux diurnal cycle favors convection through modulating the boundary layer, making the second peak more favorable for intensification.

Chapter 4

Discussion

4.1 A conceptual model for diurnally modulated overland intensification

The results from this study highlight the complex web of effects that can affect TCs as they move overland in ways that differ from behavior over oceanic surfaces. Because post-landfall TC diurnal variability remains relatively unexplored, the relative roles of radiative forcing, surface fluxes, boundary-layer evolution, and storm structure were not obvious. However, this case study indicates that the overland evolution of TS Erin, while exhibiting a nocturnal preference, cannot be explained by a single mechanism. Instead, a two-pronged conceptual model emerges from the results in which the timing of rainfall-rate maxima and vortex intensification are driven by separate diurnal responses. In this framework, the radiative diurnal cycle modulates the timing of increased rainfall rate, whereas the surface-flux diurnal cycle influences the boundary layer and is associated with organized convection within the RMW, favoring vortex intensification.

The first prong in the framework is the radiative clock, which is tested through shifting the solar cycle by 12 h between the **Control** and **Diurnal** simulations. The corresponding 12-h shift in rainfall-rate timing indicates that the nocturnal timing found in the real TS Erin was driven by the diurnal cycle. While the timing of rainfall and absolute vorticity increases between the **Control** and **Diurnal** are clearly offset by 12 h in connection with the shifted solar diurnal cycle, the diurnal cycle modulates multiple processes that include diurnally varying surface fluxes, the nocturnal NLLJ, and the convective response to atmospheric radiative forcing. The imposed-surface-flux method allows for these factors to be separated, but with some nuance due presumably to the ability for the atmosphere to respond to these changes.

The results from **D_imp1**, with the surface-flux cycle and radiative cycle offset from one another, further show that the rainfall response occurs even when the NLLJ is near a minimum. Therefore, the nocturnal rainfall preference must be dictated by something beyond simply the NLLJ or the surface-flux phase. Despite the differences in surface forcing over land surfaces, TS Erin exhibits a robust rainfall response tied to the imposed radiative diurnal phase, suggesting that a radiative control on convective timing can persist over land when sufficient moisture and storm organization are maintained. The mechanism-denial experiments further support this interpretation by separating the timing of radiative forcing from the timing of surface-flux forcing, demonstrating that the nocturnal rainfall preference in TS Erin is not simply due to surface fluxes or the NLLJ alone. Rather, the simulations show that both radiative and surface-driven processes are important for modulating rainfall.

The second prong is the nocturnal boundary layer, driven by the surface-flux response to the diurnal cycle. While the radiative phase modulates the timing of rainfall rate, the vortex response is dependent on the organization of convection relative to the RMW. The experiments reveal a consistent lag between the masked mean rainfall maxima and the masked layer-mean absolute vorticity maxima due to the coupling between inner-vortex convection and vortex stretching (Figs. 3.11 and 3.12). However, rainfall maxima do not automatically produce vortex intensification. Instead, the vortex response depends on where convection occurs relative to the RMW.

The findings from Figs. 3.10, 3.11, and 3.12 support previous literature that suggests that diabatic heating primarily located within the RMW fosters the greatest intensification rates, whereas heating maximized outside the RMW is less effective at driving intensification (Musgrave et al., 2012). The organization of convection relative to the RMW provides the link to vortex intensification, with the first **D_imp1** peak illustrating how convection concentrated outside the RMW can still produce a comparable rainfall maximum in spite of a significantly weaker vortex response. While the radiative diurnal cycle primarily modulates the timing of maximum rainfall rate in our experiment, convection within the RMW is critical to generating a strong vortex response through enhanced convergence, consistent with prior theoretical work (Musgrave et al., 2012; Smith and Montgomery, 2016).

The organization of convection within the RMW also provides a plausible explanation for why the secondary **D_imp1** peak produces a stronger vortex response than the radiatively timed peak. The imposed surface-flux phase modulates the boundary layer and NLLJ evolution, which previous studies have linked to reduced turbulent mixing, enhanced moisture transport, and low-level convergence over the Great Plains (Blackadar, 1957; Holton, 1967; Bonner, 1968; Klein et al., 2016). For TS Erin, we show this pathway in Fig. 3.13, where convergence is concentrated near or within the RMW during the nocturnal boundary-layer phase, allowing for greater ascent within the RMW. We theorize that this organization occurs through nocturnal boundary-layer stabilization, which weakens turbulent mixing and favors low-level convergence, allowing convection near the RMW to more efficiently increase absolute vorticity.

Therefore, the role of the surface fluxes should not be interpreted as a WISHE-like response to a maximum in surface fluxes, due to the offset between surface-flux timing (Fig. 2.2) and vorticity maxima (Fig. 3.9). Instead, the shallower PBL and stronger low-level convergence near the RMW during the second **D_imp1** peak (Fig.

3.13) suggest that the imposed surface-flux phase modulates convection through the boundary layer. While the analysis does not explicitly isolate the role of the NLLJ in producing this convergence, the radial structure of the convergence and differences in vertical motion profiles argue against interpreting the NLLJ as the sole driver of convective organization. Rather, the NLLJ likely helped prime the environment with moisture, while the boundary-layer response to the surface-flux diurnal cycle helped determine whether that moisture and convergence were organized near the RMW.

The interpretation of these results thus reveals storm structure as an important component of the framework. The diurnal cycle influences TS Erin through both timing and structure: radiative forcing helps set the timing of rainfall, while the boundary-layer response and RMW-relative convective organization help determine whether that rainfall contributes to intensification. In this conceptual overland framework, rainfall timing and vortex intensification are related but separable responses to the diurnal cycle.

4.2 Relationship to prior interpretations of TS Erin

Previous literature on TS Erin documented several reasons why the environment was favorable for overland reintensification. Observational studies emphasized that Erin moved into an anomalously moist environment, with months of preceding rainfall and wet soils contributing to the brown ocean effect that likely supported enhanced surface fluxes and a more favorable boundary layer (Arndt et al., 2009; Kellner et al., 2012). Modeling studies further emphasized the importance of the brown ocean effect by showing that near-surface soil moisture and associated surface fluxes influenced vortex evolution (Evans et al., 2011; Kellner et al., 2012). These studies established that TS Erin intensified within an unusually favorable overland environment. However, they focused primarily on why reintensification was possible, rather than on what controlled the timing of the convective and vortex response.

The work presented in this thesis refines those interpretations by using a high-resolution, convection-permitting modeling framework designed to separate the atmospheric radiative diurnal cycle from the surface-flux and boundary-layer response. The results suggest that Erin's nocturnal rainfall preference was not solely explained by external synoptic forcing, the NLLJ, or the surface-flux phase alone. The results show that the diurnal cycle helped organize both the timing of rainfall and convective organization in a way that was favorable for vortex intensification. Thus, the prior literature helps explain why the background environment was capable of supporting inland reintensification, while the results presented here help explain why the most important rainfall and vortex responses occurred nocturnally. In this interpretation, TS Erin operated with TC-like behavior after landfall, including being linked to the radiative diurnal cycle and to the placement of convection relative to the inner vortex, despite its overland location and asymmetric structure.

4.3 Importance for the broader TC community

A majority of TC research naturally focuses on the life cycle of these storms over the ocean, providing a large breadth of information to improve predictability in the genesis-to-intensification stage. However, inland communities remain vulnerable to hazards posed by TCs, highlighting the importance of understanding TC behavior beyond their over-ocean life cycle. Often, when these storms move from ocean to land, analysis focuses on using land-based or synoptic-based frameworks. This study, however, supports that TC-specific mechanisms can provide valuable insight to their behavior in spite of land-based processes. As such, previous TC literature concepts, namely the importance of the diurnal cycle and the importance of diabatic heating within the RMW, are similarly applicable overland when environmental conditions are right. Therefore, future studies should attempt to apply ocean-based TC frameworks when possible after landfall, rather than assuming TCs overland will be governed by totally distinct mechanisms. As shown in this study, utilizing analysis techniques such as RMW-relative frameworks, the diurnal cycle of convection, and vorticity budgets provide valuable insight into overland behavior. These techniques could be leveraged in future cases as well.

However, it is important to note that these results are not necessarily universally applicable for forecasting the behavior of overland TCs. While in this case, the nocturnal rainfall maxima resulted in nocturnal intensification, forecasters should consider the location of convection relative to an observed vortex in diagnosing whether a storm inland is likely to intensify again. Additionally, this nocturnal preference is consistent with the nocturnal preference found in general tropical convection, placing an emphasis on the environment more closely resembling that of a tropical environment. As such, forecasters should also take note of environmental context, such as predecessor rainfall events, in determining whether the environment is conducive or not, which reinforces the previous literature mentioned above.

4.4 Caveats

A few limitations should be considered when interpreting the results from this study. First, this study does not identify the causal mechanism through which the atmospheric-radiative diurnal cycle drives the nocturnal rainfall maxima in TS Erin. Nevertheless, the experiment design allows the radiative diurnal cycle to be shifted independently of the imposed surface-flux phase, supporting the interpretation that the timing response for the first **D_imp1** rainfall peak is tied to the atmospheric radiative clock.

Second, the surface-flux pathway should also be interpreted with care. In reality, the surface-flux diurnal cycle is coupled to the atmospheric radiative cycle through interactions with solar heating. Our imposed-flux experiments intentionally separate these components by prescribing the **Control** surface-flux phase while shifting the atmospheric radiative phase. Our experiment design supports that the imposed **Control** surface-flux phase remains an integral part in determining the later rainfall and vortex response. However, the exact pathway connecting the surface-flux phase to inner-core convective organization is not fully isolated here. The plausible interpretation is that the surface-flux diurnal cycle helps drive the nocturnal boundary-layer transition and NLLJ evolution, which in turn can help organize low-level convergence near the RMW. Figure 3.13 supports this interpretation by showing a shallower PBL and stronger near-RMW convergence during the second **D_imp1** peak, but the experiment does not explicitly isolate the causal pathway behind the convergence response.

Finally, these results are constrained by the use of a single case study and by the sensitivity of WRF simulations to model configuration and physical parameterizations. Future work would be necessary to test whether similar radiative and surface-flux interactions occur in other post-landfall TCs, as well as conducting an idealized modeling study that can fully parse out both mechanisms.

Chapter 5

Summary and Conclusions

TS Erin was a rare case of inland intensification for a TC. Reaching peak intensity the morning of 19 August 2007 over central Oklahoma, TS Erin brought heavy nocturnal flooding and strong wind damage to the region in a highly-saturated environment. Our study replicates this rare event using a high-resolution WRF simulation that captures key elements in its overland life cycle temporally and spatially. Using targeted sensitivity tests, our study suggests that the diurnal cycle played an essential role in controlling the timing of rainfall peaks and vortex intensification in TS Erin. Through these mechanism-denial experiments, we separated the diurnal timing of atmospheric radiative forcing from the timing of surface fluxes. These experiments demonstrate that rainfall rate timing more closely follows the radiative diurnal phase peaking nocturnally, even when the imposed surface fluxes produce an NLLJ evolution more similar to the **Control** run. This indicates that the NLLJ alone does not sufficiently explain the nocturnal rainfall maximum in TS Erin and is thus unlikely to be the dominant control on rainfall rate timing.

The vortex response, however, does not always follow rainfall timing. In most sensitivity tests, increases in absolute vorticity occur at an approximate 6-h lag to rainfall rate maxima, but the first **D_imp1** rainfall peak provides an important counterexample. Despite producing a rainfall maximum, this peak is dominated by convection that maximizes outside the RMW and is not followed by an increase in low-level absolute vorticity. In contrast, rainfall peaks associated with convection maximizing within the

RMW are associated with stronger positive convergence and stronger vortex intensification. These results suggest that vortex intensification across the simulations of our experiment strongly depended on whether convection maximized within or outside of the RMW, consistent with the previous literature.

In summary, the radiative diurnal cycle appears to modulate the timing of rainfall in TS Erin, while the organization of convection relative to the RMW governs whether the associated convection facilitates vortex intensification. This distinction provides a mechanism by which nocturnal rainfall maxima may occur without vortex spin-up when convection is displaced outward relative to the RMW, and why intensification is favored when rainfall and associated convergence are organized within the RMW. A question left for future study is the physical mechanism through which direct atmospheric radiative forcing drives the nocturnal rainfall preference in this event. Additional work should also test whether similar radiative and surface-flux interactions occur in other post-landfall TCs.

Appendix A

Figure A.2 shows the domain used for the NLLJ analysis for ERA5 and the 3 radar sites used for VADs. The location was chosen to best approximate the behavior of the NLLJ without influence from TS Erin, as the storm's track passed right through typical locations of the NLLJ. For more explicit comparison, Figure A.3 shows the comparison at each VAD site and the corresponding vertical profile for ERA5. In all 3 cases, ERA5 replicates the VADs with sufficient visual comparison, indicating ERA5 is not only capturing the general NLLJ region well but also documenting the varaibility in NLLJ strength across the region at each point.

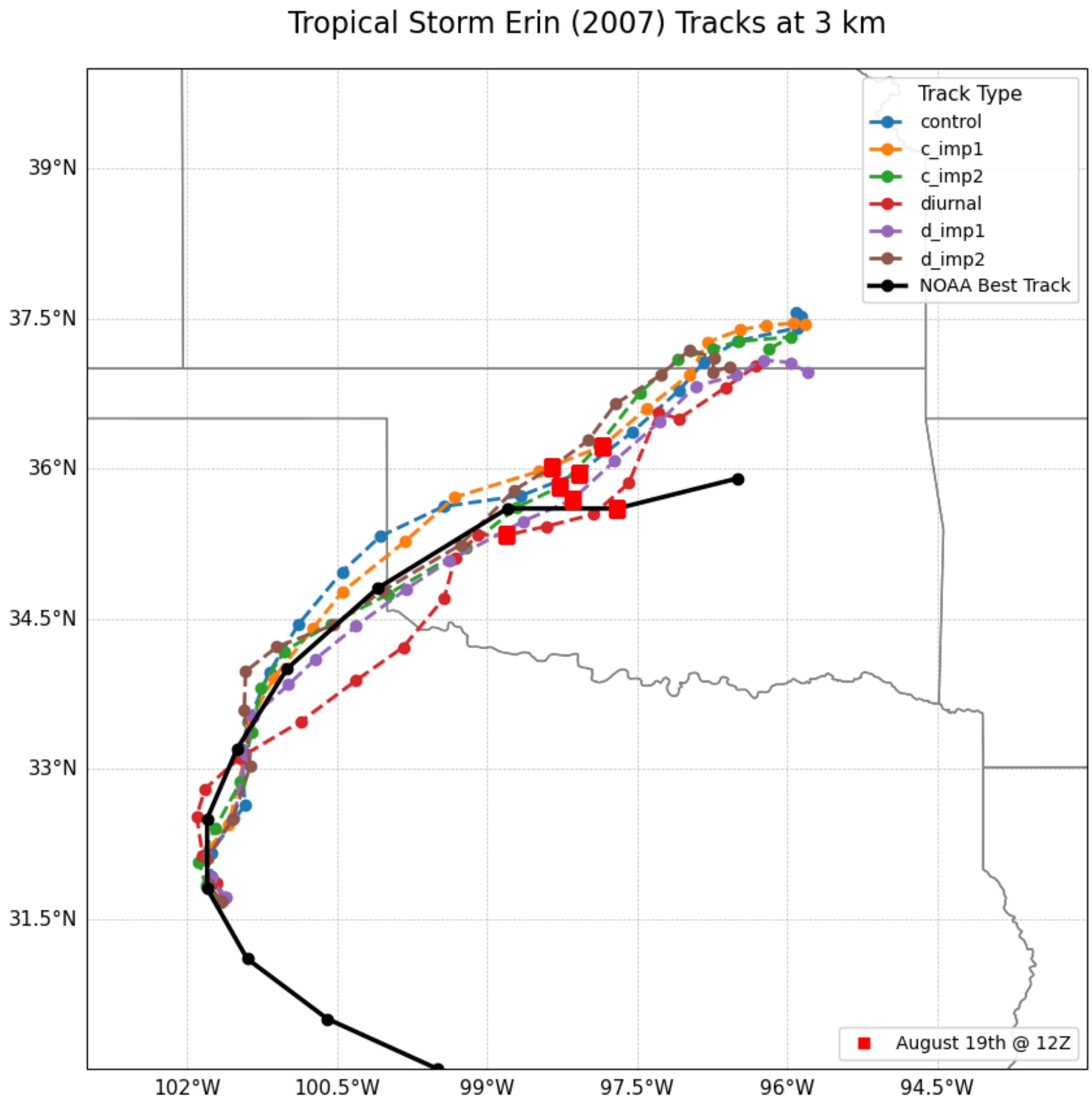

Figure A.1: Hourly track points for each simulation's iteration of Tropical Storm Erin, tracked using relative vorticity maxima, compared to NOAA Best Track (black). A common point of 19 August at 12:00 UTC is highlighted with a red box to show run-to-run temporal accuracy.

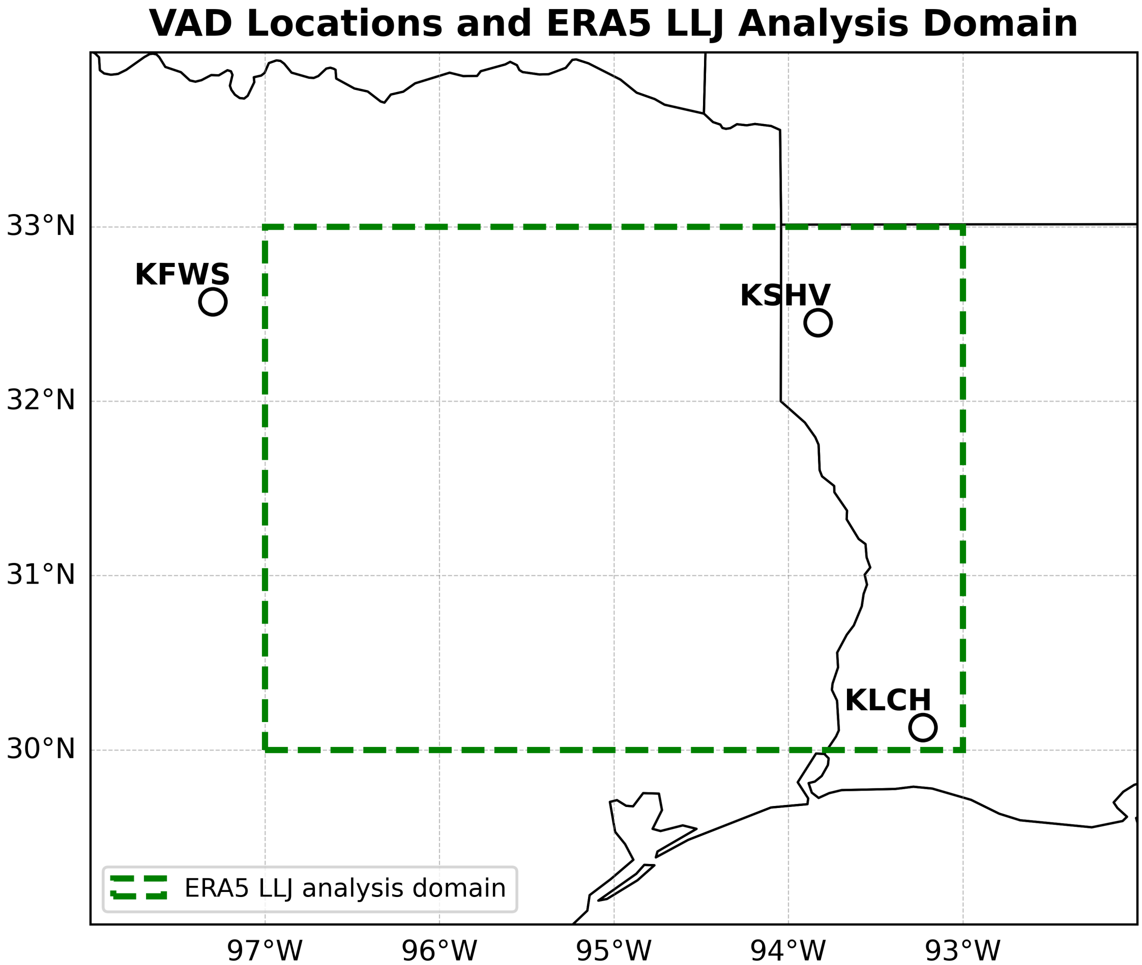

Figure A.2: ERA5 NLLJ domain used for averaging alongside locations for each radar (KFWS, KSHV, KLCH) used in vertical azimuth display (VAD) comparison analysis.

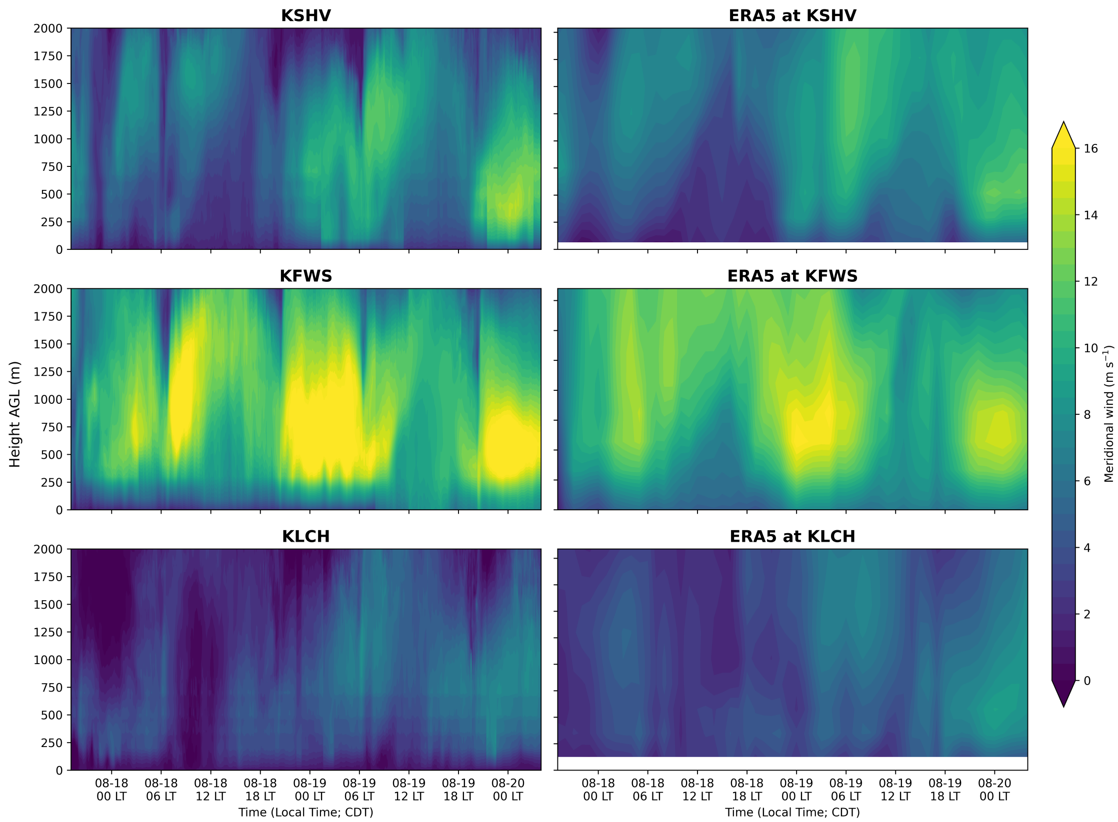

Figure A.3: Comparison of VAD time-height series (left) and corresponding time-height series using ERA5 (right). Each ERA5 plot is generated at the closest point to each radar location, demonstrating sufficient temporal, spatial, and magnitude capturing of meridional winds for ERA5 compared to observations.

Reference List

Adler, R. F., and E. B. Rodgers, 1977: Satellite-observed latent heat release in a tropical cyclone. *Monthly Weather Review*, **105 (8)**, 956–963, https://doi.org/10.1175/1520-0493(1977)105⟨0956:SOLHRI⟩2.0.CO;2.

Andersen, T. K., and J. M. Shepherd, 2014: A global spatiotemporal analysis of inland tropical cyclone maintenance or intensification. *International Journal of Climatology*, **34 (2)**, 391–402, https://doi.org/10.1002/joc.3693, URL https://onlinelibrary.wiley.com/doi/abs/10.1002/joc.3693, _eprint: https://rmets.onlinelibrary.wiley.com/doi/pdf/10.1002/joc.3693.

Arndt, D. S., J. B. Basara, R. A. McPherson, B. G. Illston, G. D. McManus, and D. B. Demko, 2009: Observations of the Overland Reintensification of Tropical Storm Erin (2007). *Bulletin of the American Meteorological Society*, **90 (8)**, 1079–1094, https://doi.org/10.1175/2009BAMS2644.1, URL https://journals.ametsoc.org/view/journals/bams/90/8/2009bams2644_1.xml.

Blackadar, A. K., 1957: Boundary layer wind maxima and their significance for the growth of nocturnal inversions. *Bulletin of the American Meteorological Society*, **38 (5)**, 283–290, https://doi.org/10.1175/1520-0477-38.5.283.

Bonner, W. D., 1968: CLIMATOLOGY OF THE LOW LEVEL JET. *Monthly Weather Review*, **96 (12)**, 833–850, https://doi.org/10.1175/1520-0493(1968)096⟨0833:COTLLJ⟩2.0.CO;2, URL https://journals.ametsoc.org/view/journals/mwre/96/12/1520-0493_1968_096_0833_cotllj_2_0_co_2.xml, section:.

Bosart, L. F., and G. M. Lackmann, 1995: Postlandfall Tropical Cyclone Reintensification in a Weakly Baroclinic Environment: A Case Study of Hurricane David (September 1979). *Monthly Weather Review*, **123 (11)**, 3268–3291, https://doi.org/10.1175/1520-0493(1995)123⟨3268:PTCRIA⟩2.0.CO;2, URL https://journals.ametsoc.org/view/journals/mwre/123/11/1520-0493_1995_123_3268_ptcria_2_0_co_2.xml.

Bowman, K. P., and M. D. Fowler, 2015: The diurnal cycle of precipitation in tropical cyclones. *Journal of Climate*, **28 (13)**, 5325–5334, https://doi.org/10.1175/JCLI-D-14-00804.1.

Brock, F. V., K. C. Crawford, R. L. Elliott, G. W. Cuperus, S. J. Stadler, H. L. Johnson, and M. D. Eilts, 1995: The Oklahoma Mesonet: A Technical Overview. *Journal of Atmospheric and Oceanic Technology*, **12 (1)**, 5–19, https://doi.org/10.1175/1520-0426(1995)012⟨0005:TOMATO⟩2.0.CO;2, URL https://journals.ametsoc.org/

view/journals/atot/12/1/1520-0426_1995_012_0005_tomato_2_0_co_2.xml.

Craig, G. C., and S. L. Gray, 1996: CISK or WISHE as the Mechanism for Tropical Cyclone Intensification. *Journal of the Atmospheric Sciences*, **53 (23)**, 3528–3540, https://doi.org/10.1175/1520-0469(1996)053⟨3528:COWATM⟩2.0.CO;2, URL https://journals.ametsoc.org/view/journals/atsc/53/23/1520-0469_1996_053_3528_cowatm_2_0_co_2.xml.

DeMaria, M., C. R. Sampson, J. A. Knaff, and K. D. Musgrave, 2014: Is Tropical Cyclone Intensity Guidance Improving? *Bulletin of the American Meteorological Society*, **95 (3)**, 387–398, https://doi.org/10.1175/BAMS-D-12-00240.1, URL https://journals.ametsoc.org/view/journals/bams/95/3/bams-d-12-00240.1.xml.

Ditchek, S. D., J. Molinari, K. L. Corbosiero, and R. G. Fovell, 2019: An Objective Climatology of Tropical Cyclone Diurnal Pulses in the Atlantic Basin. *Monthly Weather Review*, **147 (2)**, 591–605, https://doi.org/10.1175/MWR-D-18-0368.1, URL https://journals.ametsoc.org/view/journals/mwre/147/2/mwr-d-18-0368.1.xml.

Du, J., 2011: NCEP/EMC 4km gridded data (GRIB) stage iv data. NSF NCAR Earth Observing Laboratory, dataset; accessed 9 June 2026, https://doi.org/10.5065/D6PG1QDD.

Du, Y., and R. Rotunno, 2014: A simple analytical model of the nocturnal low-level jet over the great plains of the united states. *Journal of the Atmospheric Sciences*, **71 (10)**, 3674–3683, https://doi.org/10.1175/JAS-D-14-0060.1.

Dunion, J. P., C. D. Thorncroft, and C. S. Velden, 2014: The Tropical Cyclone Diurnal Cycle of Mature Hurricanes. *Monthly Weather Review*, **142 (10)**, 3900–3919, https://doi.org/10.1175/MWR-D-13-00191.1, URL https://journals.ametsoc.org/view/journals/mwre/142/10/mwr-d-13-00191.1.xml.

Ek, M. B., K. E. Mitchell, Y. Lin, E. Rogers, P. Grunmann, V. Koren, G. Gayno, and J. D. Tarpley, 2003: Implementation of Noah land surface model advances in the National Centers for Environmental Prediction operational mesoscale Eta model. *Journal of Geophysical Research: Atmospheres*, **108 (D22)**, https://doi.org/10.1029/2002JD003296, URL https://onlinelibrary.wiley.com/doi/abs/10.1029/2002JD003296, _eprint: https://agupubs.onlinelibrary.wiley.com/doi/pdf/10.1029/2002JD003296.

Emanuel, K., J. Callaghan, and P. Otto, 2008: A Hypothesis for the Redevelopment of Warm-Core Cyclones over Northern Australia*. *Monthly Weather Review*, **136 (10)**, 3863–3872, https://doi.org/10.1175/2008MWR2409.1, URL https://journals.ametsoc.org/view/journals/mwre/136/10/2008mwr2409.1.xml.

Emanuel, K. A., 1986: An Air-Sea Interaction Theory for Tropical Cyclones. Part I: Steady-State Maintenance. *Journal of the Atmospheric Sciences*, **43 (6)**, 585–605, https://doi.org/10.1175/1520-0469(1986)043⟨0585:AASITF⟩2.0.CO;2, URL https://journals.ametsoc.org/view/journals/atsc/43/6/1520-0469_1986_043_0585_aasitf_2_0_co_2.xml.

Evans, C., R. S. Schumacher, and T. J. Galarneau, 2011: Sensitivity in the Overland Reintensification of Tropical Cyclone Erin (2007) to Near-Surface Soil Moisture Characteristics. *Monthly Weather Review*, **139 (12)**, 3848–3870, https://doi.org/10.1175/2011MWR3593.1, URL https://journals.ametsoc.org/view/journals/mwre/139/12/2011mwr3593.1.xml.

Evans, R. C., and D. S. Nolan, 2022: The spatiotemporal evolution of the diurnal cycle in two WRF simulations of tropical cyclones. *Journal of the Atmospheric Sciences*, **79 (4)**, 1021–1043, https://doi.org/10.1175/JAS-D-21-0100.1.

Gray, W. M., and R. W. Jacobson, 1977: Diurnal Variation of Deep Cumulus Convection. *Monthly Weather Review*, **105 (9)**, 1171–1188, https://doi.org/10.1175/1520-0493(1977)105⟨1171:DVODCC⟩2.0.CO;2, URL https://journals.ametsoc.org/view/journals/mwre/105/9/1520-0493_1977_105_1171_dvodcc_2_0_co_2.xml.

Grell, G. A., and S. R. Freitas, 2014: A scale and aerosol aware stochastic convective parameterization for weather and air quality modeling. *Atmospheric Chemistry and Physics*, **14 (10)**, 5233–5250, https://doi.org/10.5194/acp-14-5233-2014, URL https://acp.copernicus.org/articles/14/5233/2014/.

Hersbach, H., and Coauthors, 2020: The ERA5 global reanalysis. *Quarterly Journal of the Royal Meteorological Society*, **146 (730)**, 1999–2049, https://doi.org/10.1002/qj.3803, URL https://onlinelibrary.wiley.com/doi/abs/10.1002/qj.3803, _eprint: https://onlinelibrary.wiley.com/doi/pdf/10.1002/qj.3803.

Hobgood, J. S., 1986: A Possible Mechanism for the Diurnal Oscillations of Tropical Cyclones. *Journal of the Atmospheric Sciences*, **43 (23)**, 2901–2922, https://doi.org/10.1175/1520-0469(1986)043⟨2901:APMFTD⟩2.0.CO;2, URL https://journals.ametsoc.org/view/journals/atsc/43/23/1520-0469_1986_043_2901_apmftd_2_0_co_2.xml.

Holton, J. R., 1967: The diurnal boundary layer wind oscillation above sloping terrain. *Tellus*, **19 (2)**, 199–205, https://doi.org/10.3402/tellusa.v19i2.9766.

Iacono, M. J., J. S. Delamere, E. J. Mlawer, M. W. Shephard, S. A. Clough, and W. D. Collins, 2008: Radiative forcing by long-lived greenhouse gases: Calculations with the AER radiative transfer models. *Journal of Geophysical*

Research: Atmospheres*, **113 (D13)**, https://doi.org/10.1029/2008JD009944, URL https://onlinelibrary.wiley.com/doi/abs/10.1029/2008JD009944, _eprint: https://agupubs.onlinelibrary.wiley.com/doi/pdf/10.1029/2008JD009944.

Kaplan, J., and M. DeMaria, 1995: A Simple Empirical Model for Predicting the Decay of Tropical Cyclone Winds after Landfall. *Journal of Applied Meteorology and Climatology*, **34 (11)**, 2499–2512, https://doi.org/10.1175/1520-0450(1995)034⟨2499:ASEMFP⟩2.0.CO;2, URL https://journals.ametsoc.org/view/journals/apme/34/11/1520-0450_1995_034_2499_asemfp_2_0_co_2.xml.

Kellner, O., D. Niyogi, M. Lei, and A. Kumar, 2012: The role of anomalous soil moisture on the inland reintensification of Tropical Storm Erin (2007). *Natural Hazards*, **63 (3)**, 1573–1600, https://doi.org/10.1007/s11069-011-9966-6, URL https://doi.org/10.1007/s11069-011-9966-6.

Klein, P. M., X.-M. Hu, A. Shapiro, and M. Xue, 2016: Linkages Between Boundary-Layer Structure and the Development of Nocturnal Low-Level Jets in Central Oklahoma. *Boundary-Layer Meteorology*, **158 (3)**, 383–408, https://doi.org/10.1007/s10546-015-0097-6, URL https://doi.org/10.1007/s10546-015-0097-6.

Kossin, J. P., 2002: Daily Hurricane Variability Inferred from GOES Infrared Imagery. *Monthly Weather Review*, **130 (9)**, 2260–2270, https://doi.org/10.1175/1520-0493(2002)130⟨2260:DHVIFG⟩2.0.CO;2, URL https://journals.ametsoc.org/view/journals/mwre/130/9/1520-0493_2002_130_2260_dhvifg_2.0.co_2.xml.

Lamers, A., and Coauthors, 2023: Forecasting tropical cyclone rainfall and flooding hazards and impacts. *Tropical Cyclone Research and Review*, **12 (2)**, 100–112, https://doi.org/10.1016/j.tcrr.2023.06.005, URL https://www.sciencedirect.com/science/article/pii/S2225603223000267.

Landsea, C. W., and J. L. Franklin, 2013: Atlantic hurricane database uncertainty and presentation of a new database format. *Monthly Weather Review*, **141 (10)**, 3576–3592, https://doi.org/10.1175/MWR-D-12-00254.1.

Lin, Y., and K. E. Mitchell, 2005: THE NCEP STAGE II/IV HOURLY PRECIPITATION ANALYSES: DEVELOPMENT AND APPLICATIONS. 19th Conf. on Hydrology, San Diego, CA, Amer. Meteor. Soc., 1.2., URL https://ams.confex.com/ams/pdfpapers/83847.pdf.

McPherson, R. A., and Coauthors, 2007: Statewide Monitoring of the Mesoscale Environment: A Technical Update on the Oklahoma Mesonet. *Journal of Atmospheric and Oceanic Technology*, **24 (3)**, 301–321, https://doi.org/10.1175/JTECH1976.1, URL https://journals.ametsoc.org/view/journals/atot/24/3/jtech1976_1.xml.

Musgrave, K. D., R. K. Taft, J. L. Vigh, B. D. McNoldy, and W. H. Schubert, 2012: Time evolution of the intensity and size of tropical cyclones. *Journal of Advances in Modeling Earth Systems*, **4 (3)**, https://doi.org/10.1029/2011MS000104, URL https://onlinelibrary.wiley.com/doi/abs/10.1029/2011MS000104, _eprint: https://agupubs.onlinelibrary.wiley.com/doi/pdf/10.1029/2011MS000104.

Nakanishi, M., and H. Niino, 2006: An Improved Mellor–Yamada Level-3 Model: Its Numerical Stability and Application to a Regional Prediction of Advection Fog. *Boundary-Layer Meteorology*, **119 (2)**, 397–407, https://doi.org/10.1007/s10546-005-9030-8, URL https://doi.org/10.1007/s10546-005-9030-8.

Ruppert, J. H., and C. Hohenegger, 2018: Diurnal Circulation Adjustment and Organized Deep Convection. *Journal of Climate*, **31 (12)**, 4899–4916, https://doi.org/10.1175/JCLI-D-17-0693.1, URL https://journals.ametsoc.org/view/journals/clim/31/12/jcli-d-17-0693.1.xml.

Ruppert, J. H., and M. E. O'Neill, 2019: Diurnal Cloud and Circulation Changes in Simulated Tropical Cyclones. *Geophysical Research Letters*, **46 (1)**, 502–511, https://doi.org/10.1029/2018GL081302, URL https://onlinelibrary.wiley.com/doi/abs/10.1029/2018GL081302, _eprint: https://onlinelibrary.wiley.com/doi/pdf/10.1029/2018GL081302.

Schubert, W. H., and J. J. Hack, 1982: Inertial stability and tropical cyclone development. *Journal of the Atmospheric Sciences*, **39 (8)**, 1687–1697, https://doi.org/10.1175/1520-0469(1982)039⟨1687:ISATCD⟩2.0.CO;2, URL https://journals.ametsoc.org/view/journals/atsc/39/8/1520-0469_1982_039_1687_isatcd_2_0_co_2.xml.

Skamarock, W. C., and Coauthors, 2019: A description of the advanced research wrf version 4. NCAR Technical Note NCAR/TN-556+STR, National Center for Atmospheric Research, 145 pp. https://doi.org/10.5065/1dfh-6p97.

Smith, R. K., and M. T. Montgomery, 2016: The efficiency of diabatic heating and tropical cyclone intensification. *Quarterly Journal of the Royal Meteorological Society*, **142 (698)**, 2081–2086, https://doi.org/10.1002/qj.2804, URL https://rmets.onlinelibrary.wiley.com/doi/10.1002/qj.2804.

Tewari, M., and Coauthors, 2004: Implementation and verification of the unified noah land surface model in the wrf model. *Bulletin of the American Meteorological Society*, 2165–2170, combined Preprints: 84th American Meteorological Society Annual Meeting, Seattle, WA, 11–15 January 2004.

Thompson, G., and T. Eidhammer, 2014: A Study of Aerosol Impacts on Clouds and Precipitation Development in a Large Winter Cyclone. *Journal of the Atmo-*

spheric Sciences, **71 (10)**, 3636–3658, https://doi.org/10.1175/JAS-D-13-0305.1, URL https://journals.ametsoc.org/view/journals/atsc/71/10/jas-d-13-0305.1.xml.

Thompson, G., P. R. Field, R. M. Rasmussen, and W. D. Hall, 2008: Explicit Forecasts of Winter Precipitation Using an Improved Bulk Microphysics Scheme. Part II: Implementation of a New Snow Parameterization. *Monthly Weather Review*, **136 (12)**, 5095–5115, https://doi.org/10.1175/2008MWR2387.1, URL https://journals.ametsoc.org/view/journals/mwre/136/12/2008mwr2387.1.xml.

Wang, Z., 2012: Thermodynamic aspects of tropical cyclone formation. *Journal of the Atmospheric Sciences*, **69 (8)**, 2433–2451, https://doi.org/10.1175/JAS-D-11-0298.1.

Weickmann, H. K., A. B. Long, and L. R. Hoxit, 1977: Some Examples of Rapidly Growing Oceanic Cumulonimbus Clouds. *Monthly Weather Review*, **105 (4)**, 469–476, https://doi.org/10.1175/1520-0493(1977)105⟨0469:SEORGO⟩2.0.CO;2, URL https://journals.ametsoc.org/view/journals/mwre/105/4/1520-0493_1977_105_0469_seorgo_2_0_co_2.xml.

Wu, Q., J. Hong, and Z. Ruan, 2020: Diurnal variations in tropical cyclone intensification. *Geophysical Research Letters*, **47 (23)**, e2020GL090 397, https://doi.org/10.1029/2020GL090397.

Xu, Y., 2013: Maintenance of Tropical Cyclone Bill (1988) after landfall. *Acta Meteorologica Sinica*, **27 (4)**, 486–501, https://doi.org/10.1007/s13351-013-0412-4, URL https://doi.org/10.1007/s13351-013-0412-4.

Zhang, F., and K. Emanuel, 2016: On the Role of Surface Fluxes and WISHE in Tropical Cyclone Intensification. *Journal of the Atmospheric Sciences*, **73 (5)**, 2011–2019, https://doi.org/10.1175/JAS-D-16-0011.1, URL https://journals.ametsoc.org/view/journals/atsc/73/5/jas-d-16-0011.1.xml.

Zhang, F., Z. Pu, and C. Wang, 2021: Land-surface diurnal effects on the asymmetric structures of a postlandfall tropical storm. *Journal of Geophysical Research: Atmospheres*, **126 (1)**, e2020JD033 842, https://doi.org/10.1029/2020JD033842.

Zhang, J., and Y. Du, 2025: Revisiting the diurnal pulses of tropical cyclones over the northwest pacific ocean. *Geophysical Research Letters*, **52 (14)**, e2025GL116 554, https://doi.org/10.1029/2025GL116554.

Zhang, J. A., J. P. Dunion, and D. S. Nolan, 2020: In situ observations of the diurnal variation in the boundary layer of mature hurricanes. *Geophysical Research Letters*, **47 (3)**, e2019GL086 206, https://doi.org/10.1029/2019GL086206.